Multiple structural architectures of archaeal homolog of proteasome-assembly chaperone

Arunima Sikdar

Doctor of Philosophy

Department of Functional Molecular Science
School of Physical Sciences
SOKENDAI (The Graduate University for Advanced Studies)

Multiple structural architectures of archaeal homolog of proteasome-assembly chaperone

Arunima Sikdar

Department of Functional Molecular Science

School of Physical Sciences

SOKENDAI (The Graduate University for Advanced Studies)

2017 March

A dissertation submitted for the degree of Doctor of Philosophy

List of published thesis

The chapter 2 of this doctoral thesis is a reprint of the material as it appears in "Crystal structure of archaeal homolog of proteasome-assembly chaperone PbaA" as listed below. The co-author listed in this publication directed and supervised the research that forms the basis for the doctoral thesis."

Arunima Sikdar, Tadashi Satoh, Masato Kawasaki and Koichi Kato
Crystal structure of archaeal homolog of proteasome-assembly chaperone PbaA. *Biochem Biophys. Res. Commun*. **453**: 493-497 (2014).

Abbreviations:

COOT: Crystallographic Object-Oriented Toolkit

DTT: Dithiothreitol

EM: Electron microscope

HS-AFM: High-speed atomic force microscopy

IPTG: Isopropyl β-$_{D}$-1-thiogalactopyranoside

MAD: Multi-wavelength anomalous dispersion

PAC1: Proteasome assembling chaperone 1

PAC2: Proteasome assembling chaperone 2

Pba: Proteasome biogenesis associated

SAXS: Small-angle X-ray scattering

SANS: Small-angle neutron scattering

Trx: Thioredoxin

Thesis contents:

Chapter 1: General Introduction

Chapter1: General introduction

1.1 Divergence and convergence of protein structures

The naturally evolved protein biomolecules are highly sophisticated in structures with diverse properties. Majority of these biomolecules function in integrative systems rather than acting by itself. Most often these elements can interact with the external environment to form supramolecular complex architectures. The biomolecular assemblies are highly dynamic in nature and essentially contribute to regulation of diverse array of integrated cellular functions. To interpret the biological significance of those molecular assemblies in living systems, it is important to characterize their structural architectures and dynamics in detail (Luo et al., 2014).

In general, it is assumed that high sequence identity would give rise to similar structure and function (Chothia and Lesk, 1986). YgdK from *E. coli* shares 35% sequence identity with the *E. coli* protein SufE. Both are key components for Fe-S metabolism, exhibiting the same distinct fold, and belong to a family of at least 70 prokaryotic and eukaryotic sequence homologs. In this case 35% sequence identity was enough for exhibiting same distinct fold and function (Liu et al., 2005). By contrast, many examples have been described of homologous proteins sharing common, distinct fold and function with sequence identity less than 20%. For example, the structural

characterization of the Trm9-Trm112 tRNA MTase complex revealed the structural plasticity allowing Trm112 to interact through a very similar mode with MTase partners that share less than 20% sequence identity (Letoquart et al., 2015).

However, there are exceptions of proteins having higher sequence identity but different structure and functions. For example, the two paralogs Grp94 and Hsp90 exhibit a high degree of sequence similarity (73-81%), but there are significant differences in their quaternary conformations and ATPase activity (Maharaj et al., 2016). This evidence indicates that the sequence similarity is not enough to predict functions of proteins. Therefore, determination of structure and dynamics of protein is really necessary not only to understand their physiological functions but also to artificially optimize their structural mechanisms for designated functions. In such context, I have chosen proteasome system as model for the structural study.

1.2 Proteasome system and its components

The proteasome forms a supramolecular protein complex and acts as a proteolytic machine for selective protein degradation that regulates various biological processes including cell cycle, differentiation, DNA repair, transcriptional regulation, and antigen presentation (Baumeister et al., 1998; Coux et al., 1996; Tanaka, 2009). The

fundamental component of proteasome is a barrel-shaped 20S core particle, which is responsible for the proteolytic activity. This 20S core particle is a precise proteolytic machine, layout of which is further categorized into four stacked heptameric rings of α and β subunits with a central cavity (Lowe et al., 1995; Unno et al., 2002) (**Figure 1.2.1**). To avoid nonselective proteolysis, substrate entry is restricted by a gating pore at the center of α subunit rings (Glickman, 2000; Stadtmueller and Hill, 2011). Opening of the gate, which permits the entry of unfolded polypeptides through the narrow channel, is promoted by the docking of proteasome activators (**Figure 1.2.1**) through the C-terminal HbYX (hydrophobic-tyrosine-X) motif over the α-ring (Rabl et al., 2008; Smith et al., 2007).

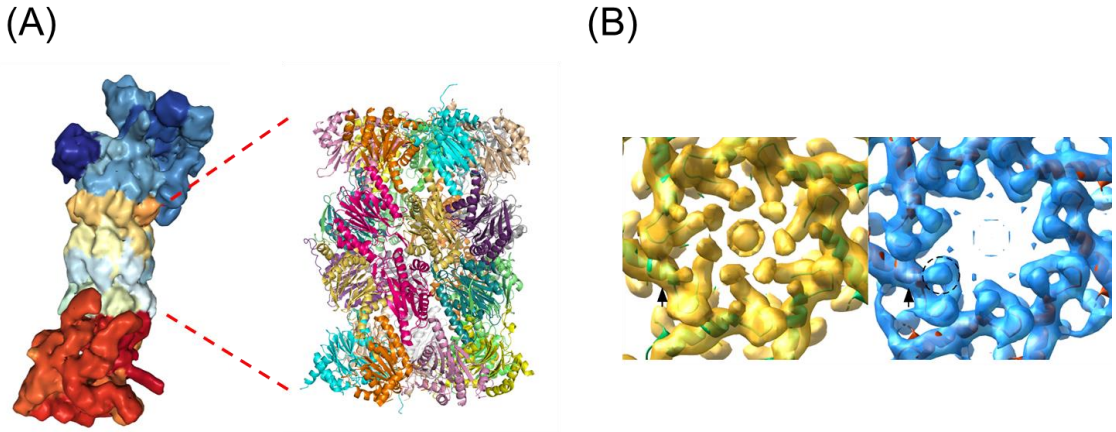

Figure 1.2.1 Three-dimensional structural views of proteasomes. (A) EM structure of the eukaryotic 26S proteasome (PDB code: 3GJR). The 20S proteasome is shown by ribbon model and highlighted in right. (B) Close-up view of gating pore of the 20S proteasome. The gate structures in the absence and presence of proteasome activator are shown in left and right, respectively.

Accumulated evidence has revealed that formation of the eukaryotic 20S proteasome is not a spontaneous process but requires at least five proteins (Pba1, Pba2, Pba3, Pba4, and Ump1) operating as assembly chaperones (Murata et al., 2009; Ramos and Dohmen, 2008). For example, the assembly chaperone proteins Pba1 and Pba2 form a heterodimer that acts as a matchmaker for the α-ring formation during the eukaryotic 20S proteasome biogenesis (Kock et al., 2015; Stadtmueller et al., 2012; Wani et al., 2015) (**Figure 1.2.2**). Pba1 and Pba2 exhibit structural similarity despite their low sequence identity (11.4%). In contrast to the eukaryotic proteasomes, archaeal 20S proteasomes are usually composed of only one type each of α and β subunits, which spontaneously assemble into four-stacked homoheptameric rings *in vitro* (Lowe et al., 1995; Sprangers and Kay, 2007) without any assistance from the chaperones and probably also in archaeal cells. Interestingly, recent bioinformatic analysis has identified PbaA and PbaB as Pba1-Pba2 homologs in archaea, *Methanococcus maripaludis*, although their sequence identities are in the range 11.3-13.6% (Kusmierczyk et al., 2011). It was reported that the *M. maripaludis* PbaA preferentially interacts with an immature 20S proteasome retaining β subunit propeptide through the conserved proteasome-binding HbYX motif. However, it is enigmatic how these archaeal

homologs are involved in proteasome assembly, which presumably proceeds in an autonomous fashion in archaeal cells.

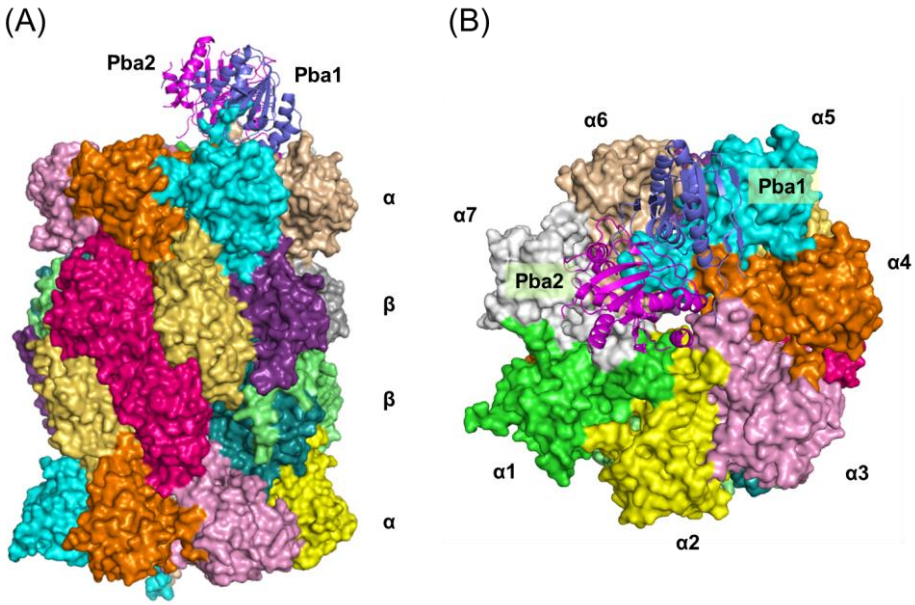

Figure 1.2.2 Structures of the 20S proteasome complexed with eukaryotic proteasome assembly chaperones Pba1 and Pba2 heterodimer (PDB code: 4G4S): (A) side view, (B) top view. The proteasome subunits and the assembly chaperone are shown as surface and ribbon models, respectively. Pba1 and Pba2 are colored by slate and magenta, respectively.

A recent study in our group has revealed that PbaB from archaeal species *Pyrococcus furiosus* exerts a dual function as an ATP-independent proteasome activator and a molecular chaperone through its tentacle-like C-terminal segments containing HbYX motif (Kumoi et al., 2013). In spite of the low sequence identities against Pba1 and

Pba2 proteins (8.0-8.3%), the overall structure of the PbaB protomer is very similar to those of Pba1 and Pba2. Unlike Pba1-Pba2 heterodimer, PbaB does not make a complex with PbaA, but instead forms a homotetrameric structure (**Figure 1.2.3**). Moreover, this study suggested that PbaA does not interact with the 20S proteasome despite of the presence of HbYX motif. Therefore, these findings raised questions as to why the HbYX-motif containing PbaA cannot bind to the proteasome and what is the functional role of this protein in archaeal cells. Moreover, it has been known that PbaA forms a complex with an unknown function protein designated as PF0014 in *P. furiosus* (Hura et al., 2009; Menon et al., 2009).

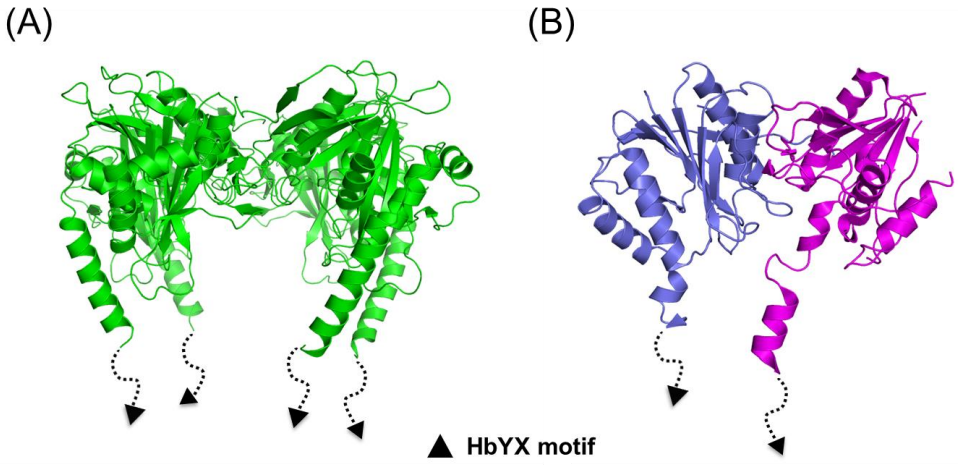

Figure 1.2.3 Crystal structures of archaeal homolog of assembly chaperone PbaB and Pba1-Pba2. The homotetrameric structures of PbaB (PDB code: 3VR0) is shown as green ribbon model, while the heterodimeric structure of Pba1 and Pba2 (PDB code: 4G4S) is colored by slate and magenta, respectively. Their C-terminal HbYX motifs are labeled with black triangle.

1.3 Scope of this study

Although it has been demonstrated that one archaeal homolog of proteaome assembly chaperone PbaB acts as a proteasome activator (Kumoi et al., 2013), it remains unclear what is the functional role of the another homolog PbaA together with the putative binding partner protein PF0014 in the archaeal cells (Hura et al., 2009; Menon et al., 2009). To address this issue, detailed structural characterization about these protein structures is necessary because the simple structural homology thus cannot estimate and explain their functions. That is why I was highly motivated to provide the structural insights into the archaeal homologs of proteasome-assembly chaperone in my PhD thesis. Such structural revelation could also offer a key clue about how the structural features of molecular assembly chaperones are shared between archaea and eukaryotes from a viewpoint of the molecular evolution. I attempted to characterize the structural features of PbaA together with the PF0014 protein by an integrative structural analysis using X-ray crystallography, high-speed atomic force microscopy (HS-AFM), native mass spectrometry, electron microscopy (EM), and solution scattering.

Chapter 2. Structural characterization of PbaA

Chapter 2. Structural characterization of PbaA

2.1 Introduction

In my research, I have focused on unveiling the structural details of archaeal homolog of assembly chaperone PbaA. Both PbaA and its archaeal homolog PbaB, which shares a common conserved proteasome-binding C-terminal HbYX motif (Kumoi et al., 2013). However, it is unexplainable how these homologs are involved in assembly of proteasome, which can proceed spontaneously *in vitro* (Lowe et al., 1995; Sprangers and Kay, 2007) and probably also in archaeal cells. Recent study revealed that the archaeon *P. furiosus* PbaB acts as an ATP-independent proteasome activator (Kumoi et al., 2013). Furthermore, the biochemical data showed that PbaA did not bind to the 20S proteasome despite its proteasome-binding HbYX motif. These findings raised questions as to why the HbYX motif-containing PbaA is not able to bind the proteasome and what is the functional role of this protein in archaeal cells. To address these issues, I have performed a crystallographic study of *P. furiosus* PbaA.

2.2 Material and methods

2.2.1 Expression and purification of PbaA

P. furiosus genomic DNA was provided from RIKEN BioResource Center (Japan).

For purification of *P. furiosus* PbaA, the gene encoding full-length PbaA (PF0015, residues 1–242) was cloned into the *Nde*I and *Xho*I sites of the pET-28b vector (Novagen). The expressed proteins contained a hexahistidine-tag at the N-terminus. *Escherichia coli* BL21 (DE3) transformed with the plasmid was cultured in LB medium containing 15 mg/L kanamycin and subsequently harvested after induction with 0.5 mM isopropyl β-D-thiogalactoside (IPTG, Wako Pure Chemical Industries) for 3 h at 37°C. Harvested cells were resuspended with buffer A [20 mM Tris-HCl (pH 8.0) and 150 mM NaCl] and lysed with sonication. The cell lysate was loaded on a Ni^{2+}-charged Chelating Sepharose column (GE Healthcare), and the bound protein fraction was extensively washed with buffer A supplemented with 20 mM imidazole. The hexahistidine-tagged protein was eluted with buffer A containing 500 mM imidazole. The eluted protein was then dialyzed against buffer B [50 mM Tris-HCl (pH 8.0)]. The protein was purified on a HiTrapQ HP anion exchange column (GE Healthcare) in buffer B containing 2 mM dithiothreitol (DTT) and developed with a 0 - 2.0 M NaCl gradient. Further purification was performed using a HiLoad Superdex 200 column (GE Healthcare) in buffer B containing 2 mM DTT and 150 mM NaCl.

The C-terminal deletion mutant (lacking residues 213–242), CΔ30-PbaA was also constructed by standard genetic engineering techniques. Expression and purification

procedures of CΔ30-PbaA were performed as according to the protocol for purification of wild-type PbaA.

2.2.2 Crystallization of PbaA

The purified PbaA protein was concentrated to 11.0 mg /ml in 50 mM Tris–HCl (pH 8.0) and used for crystallization. The crystallization screening and optimization experiments were performed by sitting-drop and hanging-drop vapor diffusion methods, respectively. The orthorhombic crystals of PbaA were obtained in a buffer containing 1.4 M sodium citrate tribasic and 0.1 M HEPES (pH 7.5) at 20ºC for 3 days (**Figure 2.2.1**). To obtain the Pt-bound PbaA orthorhombic crystal, the native crystal was soaked into the crystallization mother liquor containing 5 mM $K_2Pt(NO_2)_4$ for 6 h using Heavy Atom Screen Pt kit (Hampton Research). In the crystallization screening, monoclinic crystals of PbaA were also obtained in a buffer containing 30% 2-methyl-2,4-pentanediol (MPD), 0.1 M sodium acetate (pH 4.6), 20 mM calcium chloride (**Figure 2.2.1**).

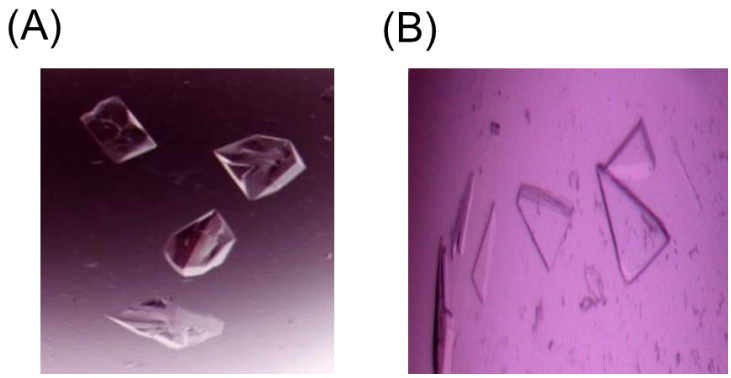

Figure 2.2.1 Single crystals of PbaA formed under the conditions of 1.4 M sodium citrate tribasic and 0.1 M HEPES (pH 7.5) (left) or 30% 2- MPD, 0.1 M sodium acetate (pH 4.6) and 20 mM calcium chloride (right).

2.2.3 X-ray diffraction data collection and structure determination

Crystals were transferred into crystallization mother liquor and stored in liquid nitrogen. The native and anomalous datasets were collected using synchrotron radiation at AR-NW12A of the Photon Factory (PF, Japan) and 13B1 of the National Synchrotron Radiation Research Center (NSRRC, Taiwan). The native dataset of the orthorhombic crystal was collected at wavelength of 0.9792 Å at PF, and the multi-wavelength anomalous dispersion (MAD) datasets were collected at wavelengths of 1.0721 Å (edge) and 1.0539 Å (high remote) at NSRRC. The dataset of the monoclinic crystal was collected at wavelength of 1.0000 Å at PF. All diffraction data were processed using HKL2000 (Otwinowski and Minor, 1997). The crystal parameters of PbaA

crystals are shown in Table 2.2.1.

The 2.80 Å-resolution structure of PbaA from the orthorhombic crystal was solved by the MAD method. The initial phase was determined using CRANK suite (Ness et al., 2004). Because the Pt-soaked and native datasets were adequately isomorphous (Table 2.21), the phase information obtained from the MAD dataset could be transferred to the native dataset. After the density modification and phase extension to 2.25 Å using DM (Cowtan, 1994), the electron density map became unambiguous enough to be interpreted. The initial models were then built automatically using ARP/wARP (Langer et al., 2008). Further manual model building into the electron density maps were conducted using COOT (Emsley et al., 2010). The refinement procedure was performed using REFMAC5 (Murshudov et al., 1997). The 2.85 Å-resolution structure of PbaA from the monoclinic crystal was solved by the molecular replacement method using the orthorhombic crystal structure of PbaA as a search model. The stereochemical qualities of the final models were validated using RAMPAGE (Lovell et al., 2003). The final refinement statistics are summarized in **Table 2.2.1** and **Table 2.2.2**. Graphic figures were prepared using PyMOL (http://www.pymol.org).

Table 2.2.1. Data collection and refinement statistics for orthorhombic crystal form of PbaA

	Native	**Edge**	**High remote**
Crystallographic data			
Space group	$C222_1$	$C222_1$	$C222_1$
Unit cell *a*/*b*/*c* (Å)	111.4/155.2/172.0	111.1/155.2/172.5	111.1/155.3/172.
Data processing statistics			
Beam line	PF-AR NW12A	NSRRC 13B1	NSRRC 13B1
Wavelength (Å)	0.9792	1.0721	1.0539
Resolution (Å)	50-2.25	30-2.80	30-2.80
Total/unique reflections	523,885/71,040	268,062/37,188	266,899/37,188
Completeness (%)	99.9 (100.0)	100.0 (100.0)	99.9 (100.0)
R_{merge} (%)	8.4 (42.1)	11.6 (72.3)	11.3 (73.6)
$I / \sigma (I)$	40.1 (6.7)	18.6 (2.6)	19.1 (2.7)
Refinement statistics			
Resolution (Å)	40.0-2.25		
R_{work} / R_{free} (%)	19.6/22.0		
R.m.s. deviations from			
Bond lengths (Å)	0.012		
Bond angles (°)	1.53		
Ramachandran plot (%)			
Favored	98.3		
Allowed	1.7		
Number of atoms			
Protein atoms (A/B/C/D/E)	1755/1772/1764/ 1764/1715		
Water molecules	308		
Average *B* factors (Å^2)			
Protein atoms	33.4/32.9/35.5/ 38.4/65.4		
Water molecules	34.1		

Table 2.2.2. Data collection and refinement statistics for monoclinic crystal form of PbaA

		Native
Crystallographic data		
Space group		$P2_1$
Unit cell	*a*/*b*/*c* (Å)	92.9/201.0/92.9
	α/β/γ(°)	90.0/110.9/90.0
Data processing statistics		
Beam line		PF-AR NW12A
Wavelength (Å)		1.0000
Resolution (Å)		50-2.85 (2.90–2.85)
Total/unique reflections		256,053/74,541
Completeness (%)		97.6 (99.9)
R_{merge} (%)		6.5 (41.1)
I / σ (I)		34.6 (4.0)
Refinement statistics		
Resolution (Å)		20.0-2.25
R_{work} / R_{free} (%)		22.6/26.4
R.m.s. deviations from		
Bond lengths (Å)		0.011
Bond angles (°)		1.35
Ramachandran plot (%)		
Favored		95.0
Allowed		5.0
Number of atoms		
Protein atoms (A~J)		1860/1860/1860/1860/1860/ 1860/1860/1860/1860/1860
Average *B* factors (Å^2)		87.1/80.2/76.5/90.6/91.9/ 89.7/92.2/94.0/80.2/82.2

2.2.4 High-speed atomic force microscopy

HS-AFM measurements of protein complexes were performed using an apparatus constructed using Prof. Ando group (Kanazawa University) (Ando et al., 2008) with cantilevers (6-7 μm long, 2 μm wide, and 90 nm thick) under the buffer solution containing 50 mM Tris-HCl (pH 8.0) and 150 mM NaCl at room temperature. The sample droplet containing 1.0 mg/ml PbaA was treated under normal mica surface. The distribution of heights of PbaA was analyzed by 2 component Gaussian fitting.

2.2.5 Negative staining electron microscopy

EM grid preparation and single particle negative staining images of the protein complexes were prepared according to the conventional protocol as previously described (Murata et al., 2010a; Murata et al., 2010b). Samples were imaged at room temperature using a JEOL JEM 2200FS electron microscope equipped with a field emission gun operating at an acceleration voltage of 200 kV. CΔ30-PbaA was dissolved at a concentration of 1.5 mg/ml in 50 mM Tris-HCl (pH 8.0) containing 150mM NaCl and 2 mM DTT.

2.2.6 Solution scattering

Solution scattering experiments were performed at 20°C during irradiation. The observed SANS and SAXS intensities were corrected for background, empty cell and buffer scatterings, and transmission factors and subsequently converted to the absolute scale by GRASP software using incident beam flux. For SANS measurements, 3.0 mg/ml PbaA was dissolved in 50 mM Tris-HCl buffer (pH 8.0) containing 150 mM NaCl and 2 mM DTT. For SAXS measurements, PbaA and CΔ30-PbaA were dissolved at concentrations of 1.0 mg/ml and 3.4 mg/ml, respectively, in 50 mM Tris-HCl buffer (pH 8.0) containing 150 mM NaCl and 2 mM DTT. The scattering intensity was normalized by weight concentration of samples.

2.3 Results

2.3.1 Crystal structures of PbaA

In the crystallization screening of *P. furiosus* PbaA, I obtained the two orthorhombic and monomeric crystals, which were diffracted up to 2.25-Å and 2.85-Å resolution, respectively. I first attempted to solve the crystal structures of *P. furiosus* PbaA by molecular replacement using the crystal structures of PbaA homologs, i.e., *P. furiosus* PbaB (PDB entry 3VR0). However, I could not find a molecular replacement solution

despite numerous trials using search models with various modifications, including homology modeling and potential loop truncations. After performing heavy atom derivatization experiments, I successfully solved the 2.25-Å resolution crystal structure by the MAD method using the Pt^{2+}-bound crystal belonging to orthorhombic space group $C222_1$ with five molecules per asymmetric unit (**Figure 2.3.1**). The final model of orthorhombic crystal form of PbaA has a R_{work} of 19.6% and R_{free} of 22.0%. Regarding the $P2_1$ monoclinic crystal, 2.85-Å resolution structure was determined by molecular replacement method. Unlike orthorhombic crystal form, ten PbaA molecules exist in the asymmetric unit. The final model of the monomeric crystal form of PbaA had a R_{work} of 22.6% and R_{free} of 26.4%.

In the orthorhombic crystal structure, N- and C-terminal residues consisting of Met1-Gly4 and Glu234-Leu242 are completely disordered. In addition, β6-β7 loop (residues Gly73-Asn76) in chain E gave no interpretable electron density. The overall chain E shows poor electron densities with high crystallographic *B* factor compared with those of chains A–D. This is probably due to the subtle crystal contact around chain E. The crystal structure of PbaA showed a pentameric structure with the contact area (825–886 $Å^2$) buried through formation of the quaternary structure. The overall structure of each PbaA protomer, which are essentially identical with a root mean square

deviation (r.m.s.d.) of 0.17–0.26 Å for superimposed 221–226 Cα atoms, exhibits a three-layered αβα fold constituted from a central eight-stranded β-sheet (β1-β3-β6-β7-β2-β8-β11-β9) flanked by two α-helices (α2 and α4) and one β-strand (β10) on one side and four α-helices (α1, α3, α5, and α6). This fold of PbaA is very similar with those of Pba1, Pba2, and PbaB (*vide infra*).

In the monoclinic crystal structure, the C-terminal segment consisting of Glu234-Leu242, which was disordered in the above mentioned orthorhombic crystal structure, became an ordered structure, i.e. 9-residues extended α6 helices (**Figure 2.3.1**). The α6 helices showed tentacle-like structures that were projected from the core domain as observed in PbaB tetramer (Kumoi et al., 2013) (*vide infra*). In contrast, the α6 helices are packed against the core in the orthorhombic crystal structure. Based on the structural properties, I designate orthorhombic and monoclinic crystal structures as "closed" and "open" forms, respectively. Upon the elongation of the α6 helices, a significant hydrophobic patch on the core domain is exposed in the cavity because the α6 helices are stabilized exclusively through hydrophobic interactions with the core in the closed form (**Figure 2.3.2**). In the crystal lattice of the open form, the α6 helices interact with each other mainly through electrostatic interaction, thereby forming a homodecameric cage-like structure (**Figure 2.3.3**). In contrast, previous analytical

ultracentrifugation data in our group showed that PbaA forms a pentamer in solution (Kumoi et al., 2013). Therefore, I supposed that the observed cage-like homodecameric structure is probably crystallographic artifact. In the crystal lattice of the closed form, the intramolecularly packed α6 helices were also involved in crystal packing (**Figure 2.3.3**). These observations prompted me to examine conformational state of PbaA in solution.

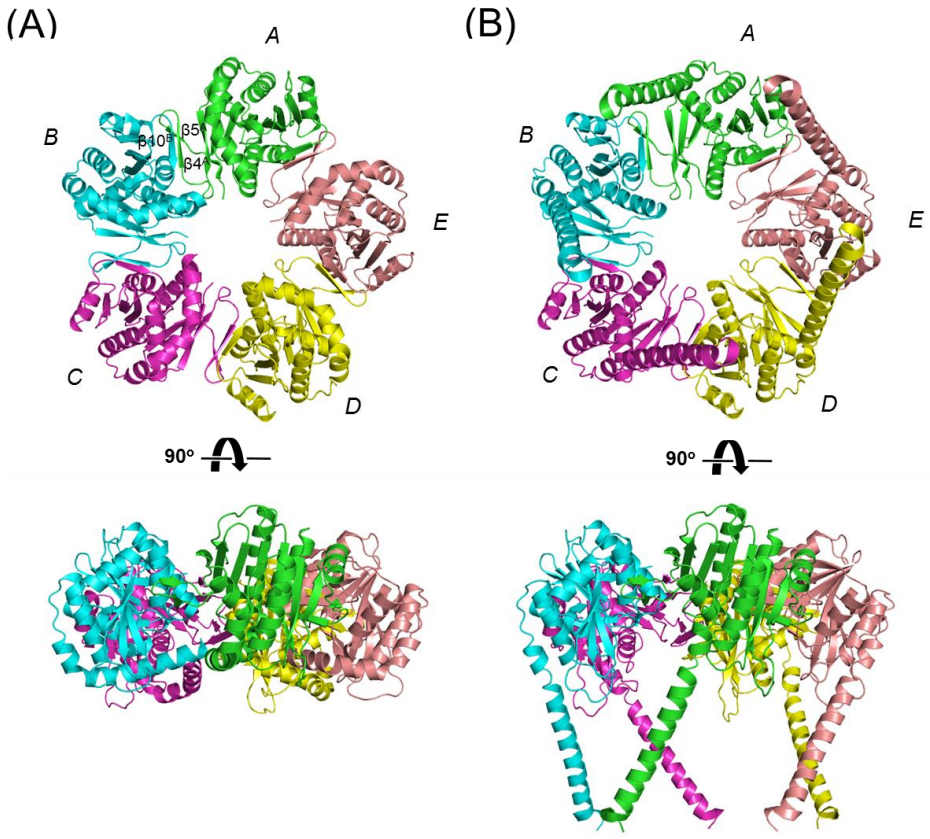

Figure 2.3.1 Ribbon models of the closed and open forms of PbaA pentamer are shown in (A) and (B), respectively. The upper and lower structures are related by a rotation of 90° around a horizontal axis. Chains A, B, C, D and E are colored green, cyan, magenta,

yellow, and pink, respectively. The β strands involved in intersubunit interaction are labeled.

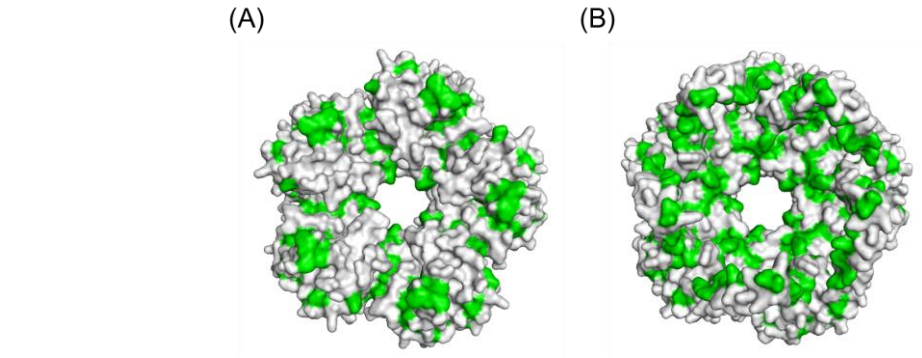

Figure 2.3.2 Surface potential representation of (A) closed and (B) open forms of PbaA. In the surface models, hydrophobic residues are colored in green.

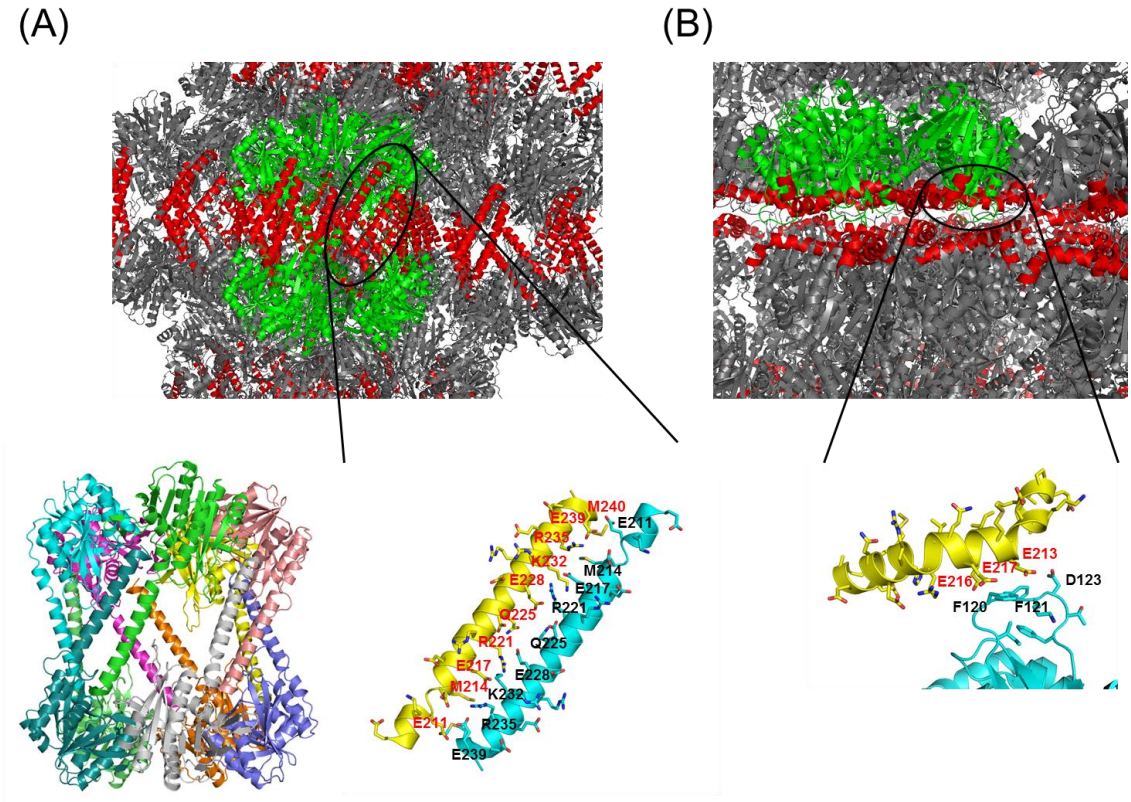

Figure 2.3.3 Crystal packing of (A) open and (B) closed forms of PbaA. Ribbon models of PbaA along with their crystallographically related molecules are shown. Ribbon

model of the extracted homodecameric cage-like structure and close-up view of intermolecular interaction mediated by the C-terminal α6 helices are shown in below. The crystallographically related molecules are colored in gray, and the C-terminal α6 helices are highlighted in red.

2.3.2 HS-AFM and solution scattering analyses of PbaA

I performed HS-AFM to characterize the PbaA conformation in solution. The HS-AFM data confirmed that PbaA exhibits a pentameric ring structure. The distribution of heights of the central position of PbaA relative to the background was analyzed from the HS-AFM images. The most frequently observed heights were estimated to be 4.5 nm (**Figure 2.3.4**), which was consistent with the height of the pentameric PbaA structure but not homodecameric cage-like structure. Additionally, although I found that there was a cavity in a brighter form, the population of such brighter form was significantly less in comparison with the other form, suggesting that the PbaA pentamer remains almost in a closed state regarding its C-terminal segments. The SANS and SAXS profiles of PbaA I obtained were remarkably similar with the profile calculated from the closed form but not with that from the open form, although there existed a significant deviation in the high *q*-range, which might be ascribed to the contribution of the minor open form (**Figure 2.3.5**). All these data indicate that the

PbaA pentamer exhibits major closed and very minor open conformations in solution.

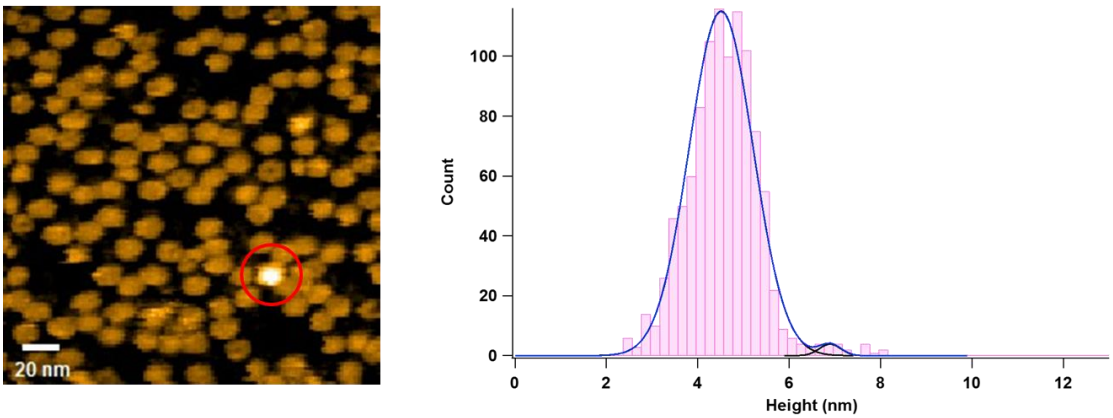

Figure 2.3.4 Typical HS-AFM image of PbaA (left). A brighter form is circled in red in HS-AFM image. Histogram and fitting of the normal distribution curve for the height between the center position of PbaA and background in the HS-AFM images (*n*=1031) (right). The heights of major peak and minor peak indicate 4.5 nm and 6.9 nm, respectively.

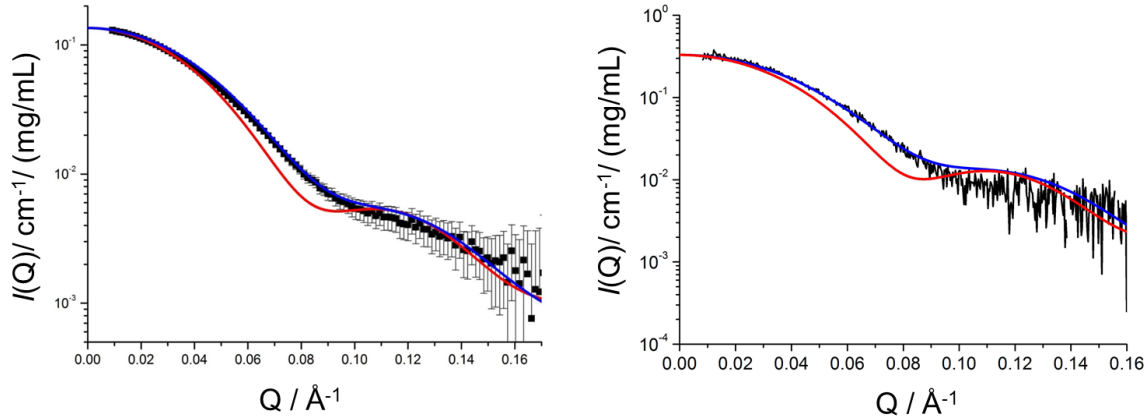

Figure 2.3.5 SANS (left) and SAXS (right) profiles calculated from the crystal structures of closed form of PbaA (blue) and open form of PbaA (red) along with the experimentally obtained profile (filled square).

As mentioned above, in the crystalline state the C-terminal segments comprising of α6 helices interacts with the core domain through hydrophobic interaction in the closed form, whereas hydrophobic patch is exposed on the surface of the core domain in the open form. To understand the structural role of the C-terminal segments of PbaA, I designed a PbaA mutant (termed CΔ30-PbaA), of which the C-terminal 30 amino acid residues were truncated, and performed its structural characterization using SAXS and electron tomography. Intriguingly, the SAXS profile showed the *Rg* values of wild-type PbaA and CΔ30-PbaA as 36.8 ± 0.3 Å and 57.5 ± 0.3 Å, respectively, which corresponded to the pentamer and a stacked dimer of the pentameric ring with C-terminal 30 amino acid residues truncation, respectively (**Fig. 2.3.6**). Consistently, the EM image of CΔ30-PbaA exhibited dimerization of the pentameric PbaA core domains, thereby suggesting that the C-terminal segments can prevent the self-dimerization of the core domains by concealing their hydrophobic surfaces (**Figure 2.3.6**).

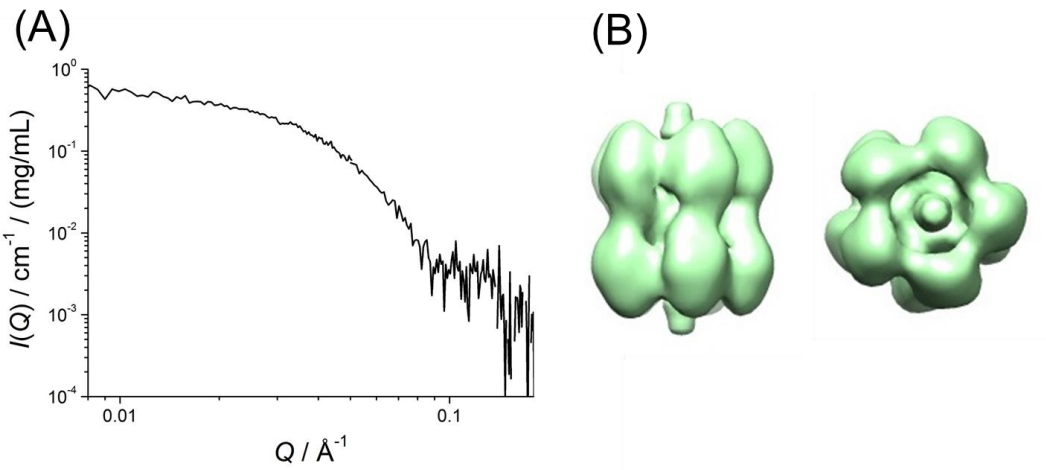

Figure 2.3.6 (A) SAXS profile of CΔ30-PbaA. (B) Three-dimensional EM images of CΔ30-PbaA from the side-view (left) and the top-view (right) were obtained by the negative staining electron microscopy.

2.4 Discussion

The overall structure of the PbaA protomer is very similar to PbaB (Kumoi et al., 2013) (**Figure 2.4.1**). The PbaA and PbaB protomers can be superimposed with r.m.s.d. of 2.21 Å for 205 Cα atoms (chain A). Despite the structural similarity of the protomers of these two proteins, their overall quaternary structures are remarkably different. The protruding β4-β5 hairpin of PbaA is responsible for the pentamerization through the formation of a three-stranded antiparallel β-sheet with β10 from the neighboring subunit. The quaternary structure difference between PbaA and PbaB is ascribed to the local conformational variation around the β4 strand and consequent difference in subunit

contact area, i.e., PbaA for 825–886 Å^2; PbaB for 1072–1184 Å^2 (**Figure 2.4.1**).

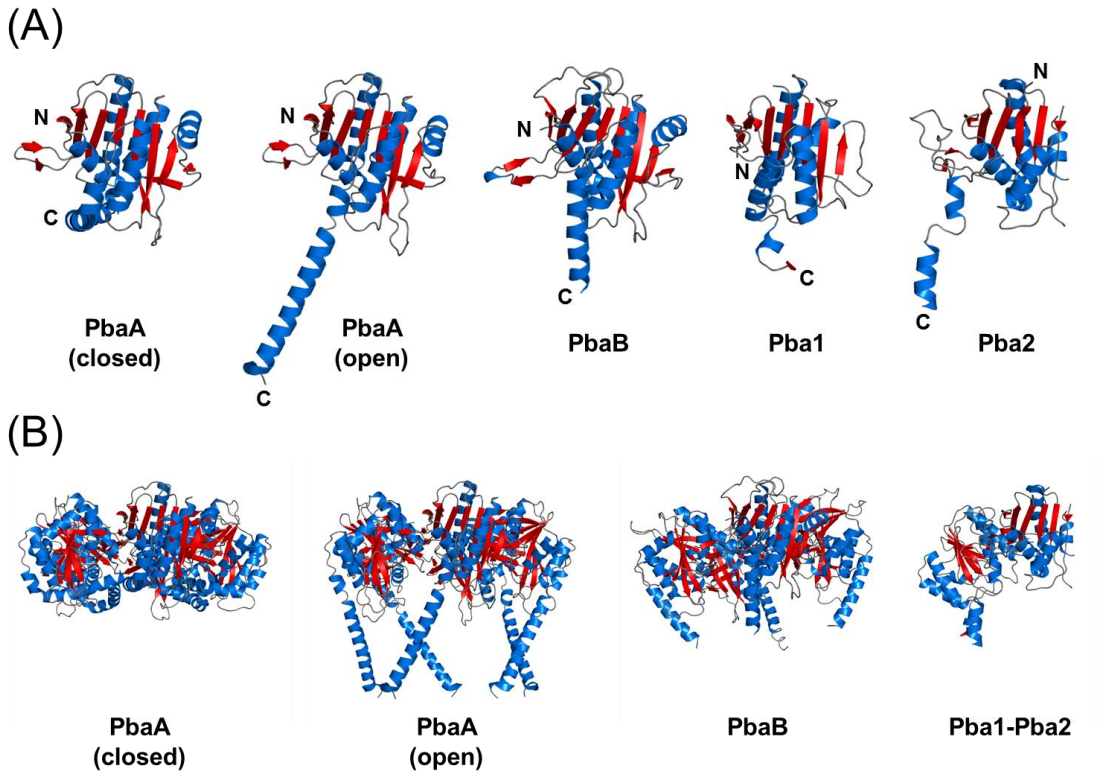

Figure 2.4.1 Comparison of ribbon models of closed and open forms of PbaA, PbaB, Pba1-2 where the β-strands, α-helices, and loops are shown in red, sky blue, and gray, respectively. The protomer structures are shown in (A), whereas their oligomeric structures are shown in (B), which are rotated by 90° around a horizontal axis.

Importantly, orientation of the C-terminal segment containing the potential proteasome-activating HbYX motif is significantly different among homopentameric PbaA, homodecameric PbaA and tetrameric PbaB (Kumoi et al., 2013) (**Figure 2.4.1**). The α6 helices of PbaB show tentacle-like structures that are projected from the core

domain and extend in the same direction. Unlike PbaA open structure; there is no significant hydrophobic patch on the surface of core domain irrespective of the C-terminal tentacle-like structure (**Figure 2.4.2**). In the pentameric PbaA, the α6 helix is stabilized primarily through hydrophobic interactions with the core along with a salt bridge between Glu216 and Arg182 (**Figure 2.3.3**). On the other hand, the protruding α6 helix of PbaB is stabilized through both hydrophobic and electrostatic interactions with Leu45/Ile215 and Lys219/Lys222 residues, respectively. The charged residue pair, Lys219 and Glu249, is conserved among archaeal PbaB homologs.

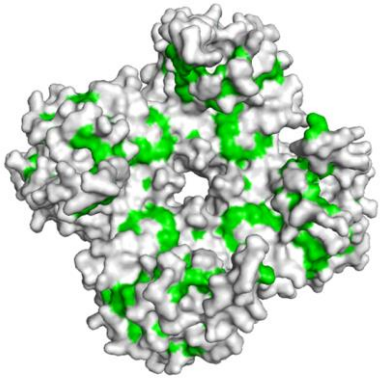

Figure 2.4.2 Surface representation of PbaB. In the surface models, hydrophobic residues are colored in green.

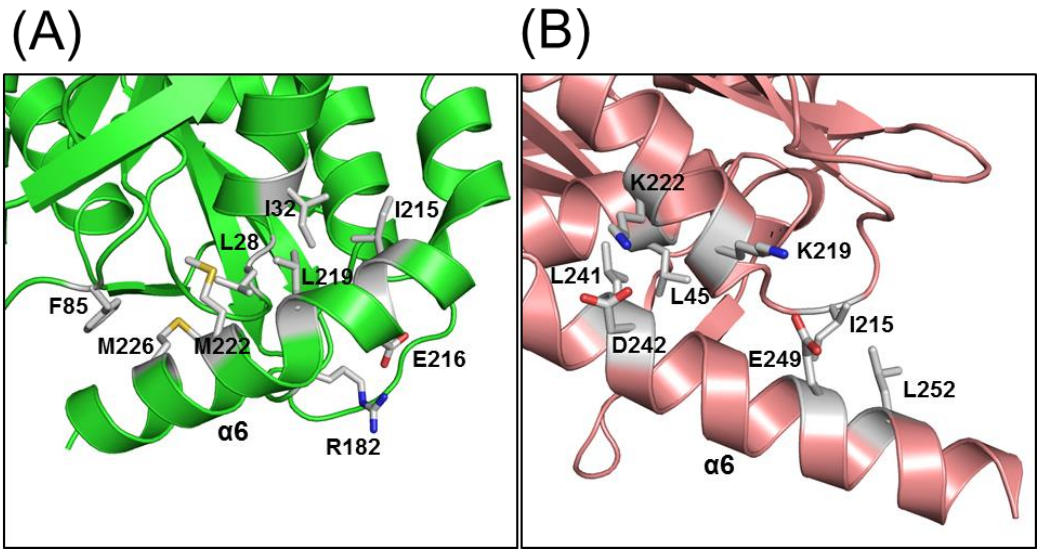

Figure 2.4.3 Close-up view of C-terminal α6 helix region of (A) PbaA and (B) PbaB. Residues involving α6 interaction are shown in the white stick model. Oxygen, nitrogen, and sulfur atoms are colored red, blue, and yellow, respectively.

Inspection of all these results revealed that the archaeal homologs of assembly chaperones PbaA and PbaB are different from the eukaryotic counterparts in terms of their oligomeric states, although their protomer core domains are structurally similar as expected from the precious bioinformatics analysis: While the eukaryotic proteasome assembly chaperones form heterodimers (Stadtmueller et al., 2012), the archaeal homologs PbaA and PbaB form homopentamer and homotetramer (Kumoi et al., 2013), respectively, even though the C-terminal proteasome-activating motifs are shared among these proteins. Furthermore, despite their similarity in domain structure, PbaA and PbaB are likely to exert distinct functions. Unlike PbaB, PbaA can exhibit

conformational transition between major closed and minor open states regarding its C-terminal segments.

Chapter 3. Creation of chimeric PbaA-PbaB with proteasome activation activity

Chapter 3. Creation of chimeric PbaA-PbaB with proteasome activation activity

3.1 Introduction

According to my results, the archaeal homologs of assembly chaperones PbaA and PbaB have different quaternary structural design from each other. Most importantly, the orientation of the C-terminal segment containing the potential proteasome-activating HbYX motif is remarkably different between PbaA and PbaB. The C-terminal α6 helices of PbaA are anchored inside the core through hydrophobic interactions, whereas the C-terminal α6 helices of PbaB showed tentacle-like structures that are projected from the core domain. These structural features may explain the distinct 20S proteasome binding abilities of archaeal homologs of proteasome-assembly chaperone: Notwithstanding the fact that the C-terminal proteasome-activating motif is conserved between PbaA and PbaB, only PbaB can activate the 20S proteasome. Based on the structural information of PbaA which I revealed, a protein engineering approach was applied with attempt to provide this protein with the binding ability to the 20S proteasome.

To examine this possibility, I created a PbaA-PbaB chimeric protein $PbaA^{N204}$-$PbaB^{C43}$, in which the entire C-terminal α6 helix of PbaA (Val205-Leu242) was replaced with that of PbaB (Met238-Leu280) (**Figure 3.1.1**). I expected that this

chimeric protein exhibit an open conformation because of decreased hydrophobic interactions between the PbaB-derived α6 helices and the core domains. As a reference, I also prepared another chimeric protein PbaA^{N230}-PbaB^{C13}, in which the crystallographically disordered C-terminal segment of PbaA (Arg231-Leu242) was replaced with the corresponding disordered residues of PbaB (Pro268-Leu280).

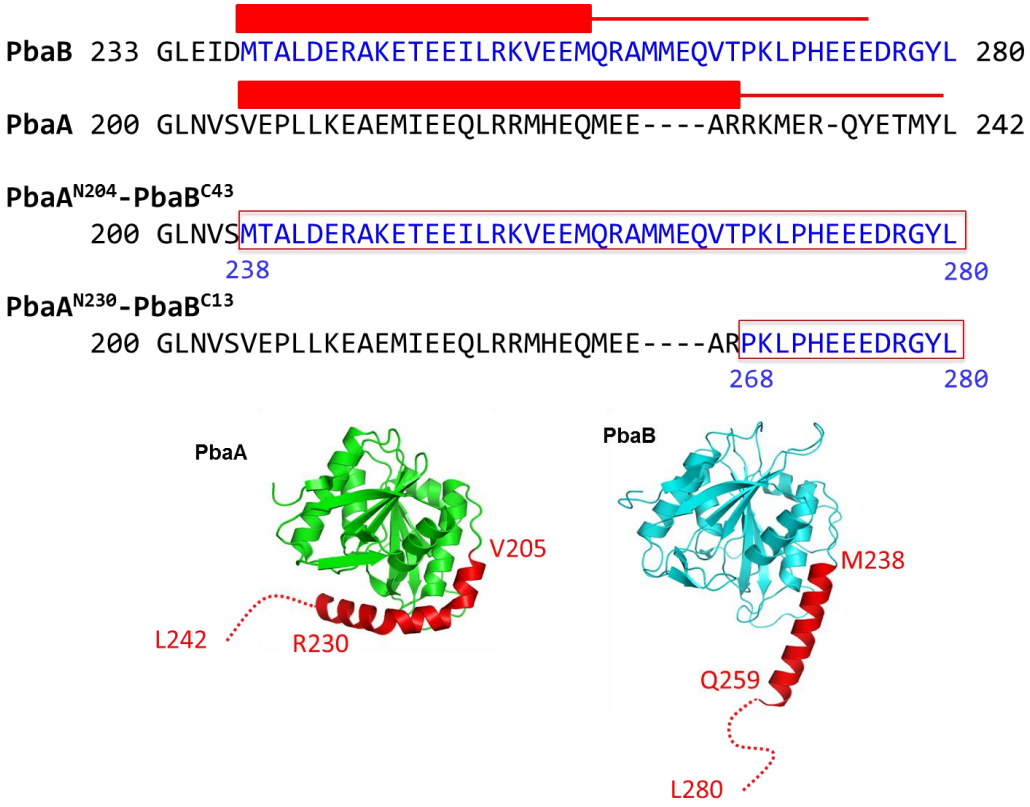

Figure 3.1.1 Amino acid sequence alignment of the C-terminal segment of PbaB, PbaA, PbaA^{N204}-PbaB^{C43} and PbaA^{N230}-PbaB^{C13} showing secondary structures (α-helices in red) and disordered regions. The crystal structures of PbaA and PbaB protomers are also indicated.

3.2 Material and methods

3.2.1 Expression and purification of PbaA

P. furiosus genomic DNA was provided from RIKEN BioResource Center (Japan). For purification of *P. furiosus* PbaA, the gene encoding full-length PbaA (PF0015, residues 1–242) was cloned into the *Nde*I and *Xho*I sites of the pET-28b vector (Novagen). The expressed proteins contained a hexahistidine-tag at the N-terminus. *Escherichia coli* BL21 (DE3) transformed with the plasmid was cultured in LB medium containing 15 mg/L kanamycin and subsequently harvested after induction with 0.5 mM isopropyl β-D-thiogalactoside (IPTG, Wako Pure Chemical Industries) for 3 h at 37°C. Harvested cells were resuspended with buffer A [20 mM Tris-HCl (pH 8.0) and 150 mM NaCl] and lysed with sonication. The cell lysate was loaded on a Ni^{2+}-charged Chelating Sepharose column (GE Healthcare), and the bound protein fraction was extensively washed with buffer A supplemented with 20 mM imidazole. The hexahistidine-tagged protein was eluted with buffer A containing 500 mM imidazole. The eluted protein was then dialyzed against buffer B [50 mM Tris-HCl (pH 8.0)]. The protein was purified on a HiTrapQ HP anion exchange column (GE Healthcare) in buffer B containing 2 mM dithiothreitol (DTT) and developed with a 0 - 2.0 M NaCl gradient. Further purification was performed using a HiLoad Superdex 200 column (GE

Healthcare) in buffer B containing 2 mM DTT and 150 mM NaCl.

Two constructs of PbaA-PbaB chimeric proteins were created by replacing the C-terminal segment of PbaA with that of PbaB. In one construct (designated as $PbaA^{N230}$-$PbaB^{C13}$), Arg231-Leu242 of PbaA was replaced by Pro268-Leu280 of PbaB. In the other construct (designated as $PbaA^{N204}$-$PbaB^{C43}$), Val205-Leu242 of PbaA was replaced by Met238-Leu280 of PbaB. Expression and purification of $PbaA^{N230}$-$PbaB^{C13}$ and $PbaA^{N204}$-$PbaB^{C43}$ were performed as according to the protocol for purification of wild-type PbaA.

3.2.2 High-speed atomic force microscopy

HS-AFM measurements of protein complexes were performed using an apparatus constructed using Prof. Ando group (Kanazawa University) (Ando et al., 2008) with cantilevers (6-7 μm long, 2 μm wide, and 90 nm thick) under the buffer solution containing 50 mM Tris-HCl (pH 8.0) and 150 mM NaCl at room temperature. Final concentrations of samples were as follows: 20S proteasome, 1.6 mg/ml; $PbaA^{N230}$-$PbaB^{C13}$, 1.9 mg/ml; $PbaA^{N204}$-$PbaB^{C43}$, 1.7 mg/ml; PbaB, 1.0 mg/ml and PbaA, 1.5 mg/ml. All samples were measured using normal mica surface. The distribution of heights of PbaA was analyzed by 2 component Gaussian fitting. In case

of HS-AFM analyses of the interaction between Pba proteins and the 20S proteasome, only the 20S proteasome was treated on the normal mica surface, then subsequently each Pba proteins were carried on it.

3.2.3 Solution scattering

Solution scattering experiments were performed at 20°C during irradiation. The observed SAXS intensity was corrected for background, empty cell and buffer scatterings, and transmission factors and subsequently converted to the absolute scale by GRASP software using incident beam flux. The scattering intensities were normalized by weight concentration of samples. Wild-type PbaA, $PbaA^{N230}$-$PbaB^{C13}$ and $PbaA^{N204}$-$PbaB^{C43}$ were dissolved at concentrations of 1.0 mg/ml, 1.9 mg/ml and 1.7 mg/ml, respectively, in buffer containing 50 mM Tris-HCl (pH 8.0), 150 mM NaCl and 2 mM DTT.

3.2.4 Proteasome activation assay

All samples were dialyzed overnight in 20 mM Tris-HCl (pH 7.5) and 150 mM NaCl. For the proteasome activation assay, 10 mM fluorogenic nonapeptide substrate [LFP, mca-AKVYPYPME-dap (dnp)-amide] was mixed with 35 nM 20S proteasome in the

presence and absence of 175 nM Pba proteins and incubated at 45ºC for 15 min with a 5-min sampling interval as previously described (Kumoi et al., 2013). Hydrolysis of the LFP was monitored at λex 330 nm and λem 398 nm.

3.3 Results

3.3.1 Structural characterization of PbaA-PbaB chimeric proteins

I performed HS-AFM and SAXS measurements to characterize the conformation of these chimeric proteins. Based on the AFM images, I confirmed that both chimeric proteins retain the homo pentameric ring architectures. The distribution of heights of the central position of the pentameric rings relative to the background was analyzed from the HS-AFM images. In PbaA^{N204}-PbaB^{C43}, the most frequently observed heights were estimated to be around 5 nm (**Figure 3.3.1**). Additionally, the population of brighter forms, of which heights were estimated to be 6.6-6.8 nm, was significantly increased in comparison with wild-type PbaA, suggesting that the open conformation of the C-terminal segments was more populated in PbaA^{N204}-PbaB^{C43}, as expected. An unexpected finding was that the open form was significantly populated also in PbaA^{N230}-PbaB^{C13}. The *Rg* values determined from SAXS profiles of wild-type PbaA, PbaA^{N230}-PbaB^{C13} and PbaA^{N204}-PbaB^{C43} were 36.8 ± 0.3 Å, 38.8 ± 0.5 Å and 41.1 ± 0.5 Å, respectively (**Figure 3.3.2**). These data also consistent with the HS-AFM results indicating that open conformations are more populated in these chimeric proteins as compared with wild-type PbaA.

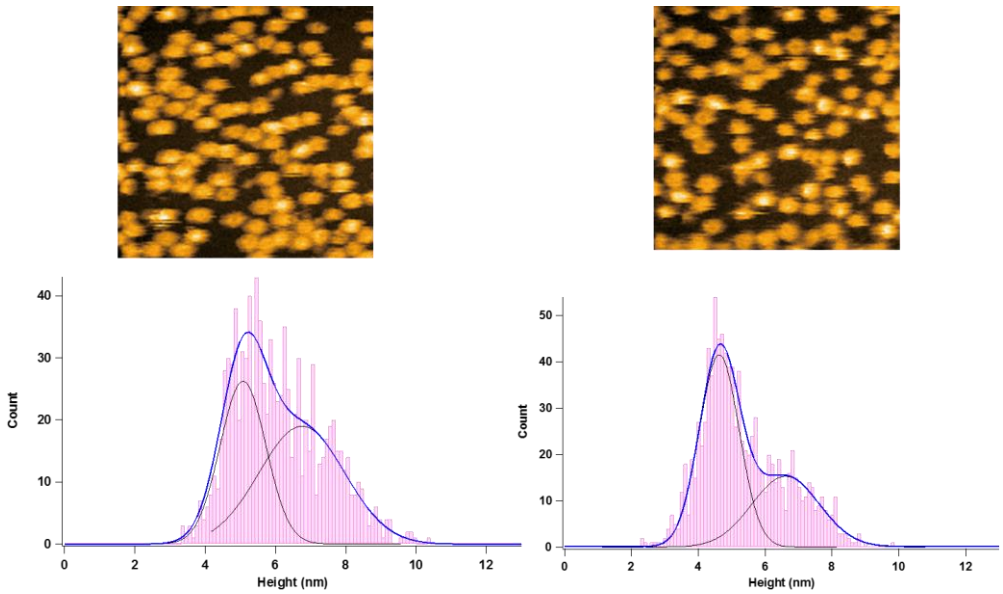

Figure 3.3.1 Typical HS-AFM images (upper) and histograms (lower) of (A)PbaA^{N204}-PbaB^{C43} (*n*=998) and (B) PbaA^{N230}-PbaB^{C13} (*n*=1028). Fitting of the normal distribution curve for the height between the center position of PbaA-PbaB chimeric proteins and background in the HS-AFM images is shown with histogram.

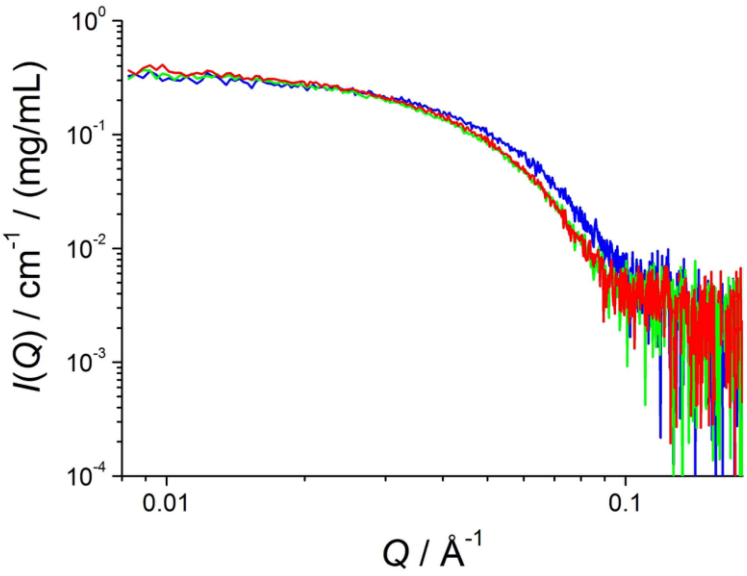

Figure 3.3.2 The experimentally obtained SAXS profiles of PbaA^{N204}-PbaB^{C43} (red), PbaA^{N230}-PbaB^{C13} (green), and wild-type PbaA (blue). The SAXS profiles yielded the *Rg* values of wild-type PbaA, PbaA^{N230}-PbaB^{C13} and PbaA^{N204}-PbaB^{C43} were 36.8 ± 0.3 Å, 38.8 ± 0.5 Å and 41.1 ± 0.5 Å, respectively

I used the HS-AFM technique also to examine a possible proteasome-binding ability of these chimeric proteins. According to the HS-AFM images, like PbaB, PbaA^{N230}-PbaB^{C13} and PbaA^{N204}-PbaB^{C43} bound to the α-ring surface of 20S proteasome, whereas wild-type PbaA did not bind to 20S proteasome (**Figure 3.3.3**).

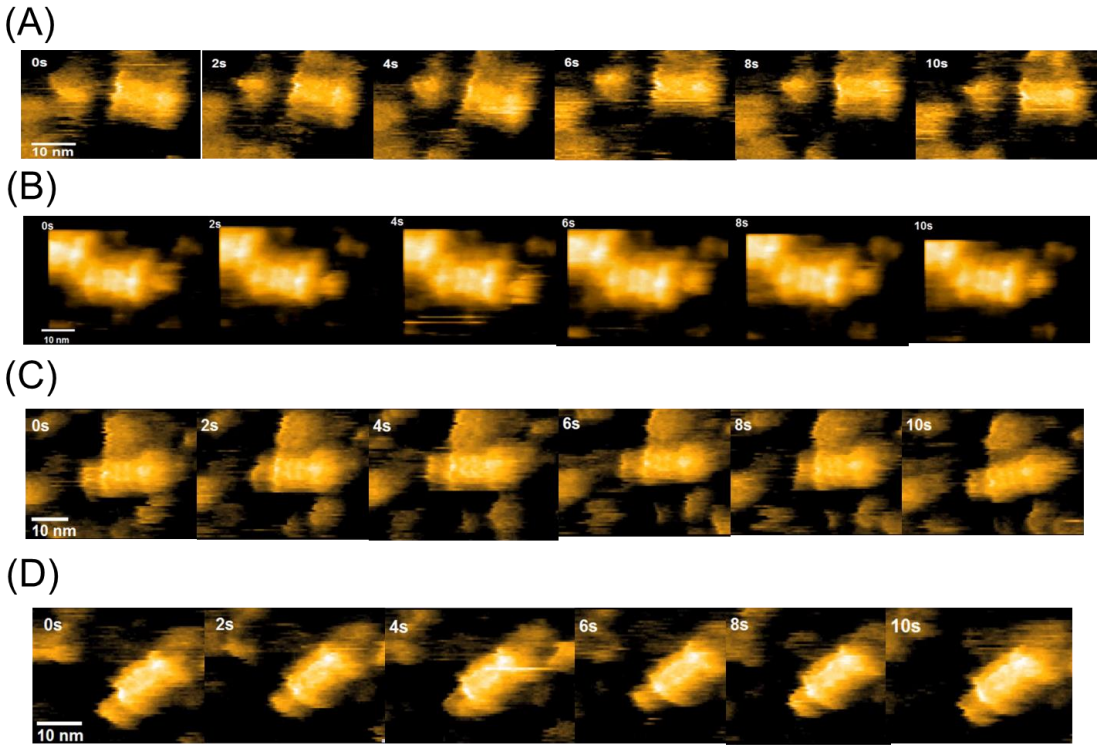

Figure 3.3.3 Typical snapshots of HS-AFM images of (A) PbaA, (B) PbaB, (C)PbaA^{N230}-PbaB^{C13} and (D)PbaA^{N204}-PbaB^{C43} at 0, 2, 4, 6, 8 and 10 sec in the HS-AFM movies.

3.3.2 Proteasome activation activities of PbaA-PbaB chimeric proteins

I ascertained whether or not PbaA-PbaB chimeric proteins could activate the 20S proteasome. As model substrates for probing possible proteasomal activation, I used a fluorogenic nonapeptie substrate (LFP, mca-AKVYPYPME-dap(dnp)-amide). In accordance with their binding activities as observed in HS-AFM image, both PbaA^{N230}-PbaB^{C13} and PbaA^{N204}-PbaB^{C43} accelerated proteasomal degradation of LFP almost equally with PbaB, whereas wild-type PbaA did not have such an activity (**Figure 3.3.4**).

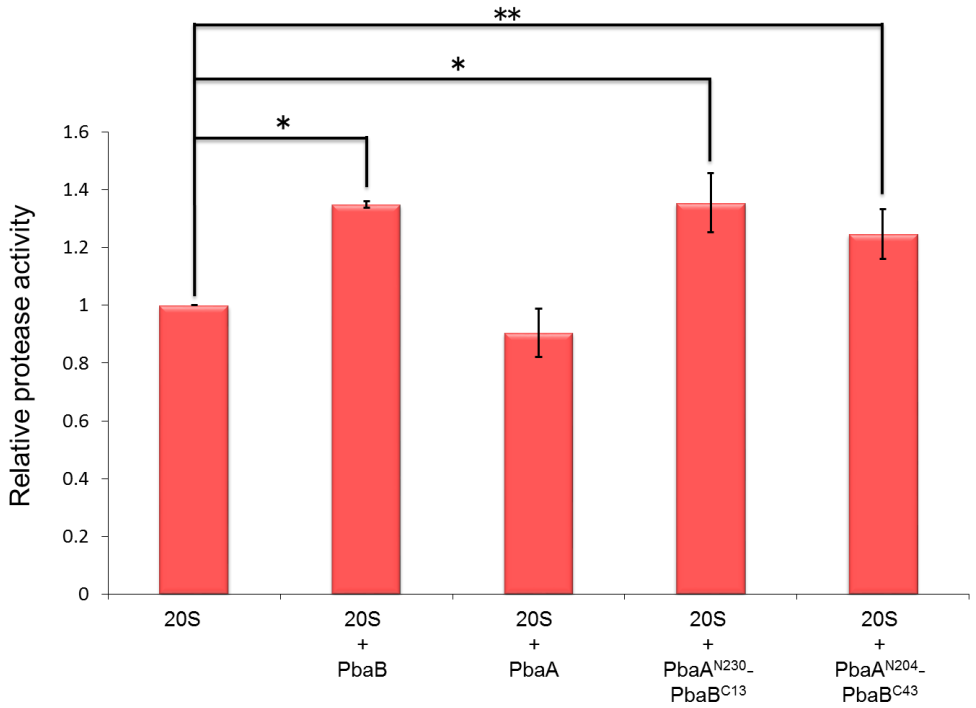

Figure 3.3.4 PbaA-PbaB chimeric proteins accelerated proteasomal degradation. Mixture of the wild-type 20S proteasome and fluorogenic nonapeptide was incubated in the presence and absence of activator candidates. Values are mean ±s.d., n=3. Statistical analyses were performed using a two-tailed unpaired Student's test, *P<0.05, **P<0.1.

3.4 Discussion

My HS-AFM data in conjunction with SAXS data indicated that the open conformation of the C-terminal segments was more populated in $PbaA^{N204}$-$PbaB^{C43}$, in which the entire C-terminal α6 helix of PbaA was replaced with that of PbaB, probably through elimination of the hydrophobic interactions. Unexpectedly, $PbaA^{N230}$-$PbaB^{C13}$, in which the crystallographically disordered C-terminal segment of PbaA was replaced with the corresponding disordered residues of PbaB, also exhibited an open conformation regarding its C-terminal segments. The C-terminal segment of PbaB harbors three successive glutamate residues, Glu273, Glu274, and Glu275 (**Fig.3.1.1**). Therefore, the electrostatic repulsion among the negatively charged C-terminal segments derived from PbaB cause the conformational opening of this chimeric protein.

Previous EM analyses in our group demonstrated that the PbaB tetramer was significantly tilted with respect to the surface of the α subunit ring (Kumoi et al., 2013). In my HS-AFM data, the PbaA-PbaB chimeric pentamers significantly fluctuated in the complex with the 20S proteasome, probably because of their partial capping of the 20S proteasome. Therefore only a subset of C-terminal segments of the chimeric proteins was directly involved in the interaction with the homoheptameric α-subunit ring of the 20S proteasome possibly due to symmetry mismatch between pentamer and heptamer.

That could be a reason why both PbaA^{N230}-PbaB^{C13} and PbaA^{N204}-PbaB^{C43} showed similar activities for the 20S proteasome to the PbaB tetramer, even though PbaA-PbaB chimeric proteins form a pentameric structure.

By inspection of all these data, I found that not only proteasome activating motif but also an open conformational state of the C-terminal segments is prerequisite for association with the 20S proteasome and thereby acting as proteasome activator. With this concept, I could successfully endow the homopentameric scaffold of PbaA with proteasome-activating activity by its chimera with the PbaB C-terminal segments.

Chapter 4. Structural characterization of PbaA/PF0014 complex

Chapter 4. Structural characterization of PbaA/PF0014 complex

4.1 Introduction

Above mentioned unique structural property of PbaA raises some questions why such disparity exists between these two structural homologs PbaA and PbaB. Namely, one homolog PbaB has an open configuration while the other homolog PbaA has primarily closed configurations, and what could be the role of flexible C-terminal segments of PbaA under the physiological condition. Such distinct structural architecture of PbaA suggests its intriguing structural mechanism associated with an as yet undiscovered function.

In fact, previous proteome and SAXS-based structural proteomics analyses revealed that PbaA forms a stable complex with an unknown function protein PF0014 (Hura et al., 2009; Menon et al., 2009). Existence of the putative binding partner protein raised possibilities that it might have some specific role in the PbaA structural design. However, there was no detailed structural information about the protein complex. Thus, I attempted to perform structural characterization of the protein complex formed between PbaA and PF0014 by several biophysical experiments including native mass spectrometry, negative staining EM analyses, and HS-AFM.

4.2 Material and methods

4.2.1 Expression and purification of PbaA

P. furiosus genomic DNA was provided from RIKEN BioResource Center (Japan). For purification of *P. furiosus* PbaA, the gene encoding full-length PbaA (PF0015, residues 1–242) was cloned into the *Nde*I and *Xho*I sites of the pET-28b vector (Novagen). The expressed proteins contained a hexahistidine-tag at the N-terminus. *Escherichia coli* BL21 (DE3) transformed with the plasmid was cultured in LB medium containing 15 mg/L kanamycin and subsequently harvested after induction with 0.5 mM isopropyl β-D-thiogalactoside (IPTG, Wako Pure Chemical Industries) for 3 h at 37°C. Harvested cells were resuspended with buffer A [20 mM Tris-HCl (pH 8.0) and 150 mM NaCl] and lysed with sonication. The cell lysate was loaded on a Ni^{2+}-charged Chelating Sepharose column (GE Healthcare), and the bound protein fraction was extensively washed with buffer A supplemented with 20 mM imidazole. The hexahistidine-tagged protein was eluted with buffer A containing 500 mM imidazole. The eluted protein was then dialyzed against buffer B [50 mM Tris-HCl (pH 8.0)]. The protein was purified on a HiTrapQ HP anion exchange column (GE Healthcare) in buffer B containing 2 mM dithiothreitol (DTT) and developed with a 0 - 2.0 M NaCl gradient. Further purification was performed using a HiLoad Superdex 200 column (GE

Healthcare) in buffer B containing 2 mM DTT and 150 mM NaCl.

CΔ30-PbaA was also constructed by standard genetic engineering techniques. Expression and purification of CΔ30-PbaA was performed as according to the protocol for purification of wild-type PbaA.

4.2.2 Expression and purification of PF0014

For purification of *P. furiosus* PF0014, the gene encoding full-length PF0014 (residues 1–128) was cloned into the *Nde*I and *Xho*I sites of the pET-28b vector. The expressed proteins contained a hexahistidine-tag at the N-terminus. *E. coli* BL21 (DE3) transformed with the plasmid was cultured in LB medium containing 15 mg/L kanamycin and subsequently harvested after induction with 0.5 mM IPTG for 12 h at 25°C. Harvested cells were resuspended with 20 mM Tris-HCl (pH 8.0), 500 mM NaCl and 5% glycerol and lysed with sonication. The hexahistidine-tagged PF0014 was purified using a Ni^{2+}-immobilized affinity column (Chelating Sepharose, GE Healthcare).

For purification of thioredoxin (Trx)-tagged PF0014, the PF0014 gene was cloned into the *Bam*HI and *Sal*I sites of the pCold-TRX vector (Subedi et al., 2012). *E. coli* BL21 (DE3) transformed with the expression plasmid was cultured in LB medium

containing 50 mg/L ampicillin and subsequently harvested after induction with 0.5 mM IPTG for 12 h at 15°C. Harvested cells were resuspended with buffer C [20 mM Tris-HCl (pH 8.0), 200 mM NaCl and 5% glycerol] and lysed with sonication. The hexahistidine-Trx-tagged PF0014 was purified using a Ni^{2+}-immobilized affinity column (Chelating Sepharose, GE Healthcare), from *E. coli* soluble lysate. The protein was washed with buffer C containing 150 mM imidazole three times consecutively. The hexahistidine-tagged protein was eluted with buffer C containing 500 mM imidazole. The eluted protein was then dialyzed against buffer D [20 mM Tris-HCl (pH 8.0)]. The protein was purified on a HiTrapQ HP anion exchange column (GE Healthcare) in buffer D containing 2 mM DTT and developed with a 0-2.0 M NaCl gradient. Further purification was performed using a HiLoad Superdex 200 column (GE Healthcare) in buffer D containing 2 mM DTT and 200 mM NaCl.

4.2.3 Purification of PbaA/PF0014 complexes

For the purification of the complex of PbaA and PF0014, both protein samples were mixed in a 1:1 molar ratio. After mixing, the complex sample was put in dialysis for 12 h using the buffer containing 50 mM Tris-HCl (pH 8.0), 200 mM NaCl and 2 mM DTT. Further purification was performed using a HiLoad Superdex 200 column (GE

Healthcare) under the same buffer condition. For the purification of PbaA/Trx-tagged PF0014 complex, the same ascribed protocol was used as according to that of non-tagged PbaA/PF0014 complex.

4.2.4 High-speed atomic force microscopy

HS-AFM measurements of protein complexes were performed using an apparatus constructed using Prof. Ando group (Kanazawa University) (Ando et al., 2008) with cantilevers (6-7 μm long, 2 μm wide, and 90 nm thick) at room temperature. PbaA/PF0014 complex was dissolved at a concentration of 1.0 mg/ml in 50 mM Tris-HCl buffer (pH 8.0) including 150 mM NaCl. The sample droplet was placed on a normal mica or a mica treated with 0.1% 3-aminopropyltriethoxysilane (aminosilane).

4.2.5 Native mass spectrometry

Native MS was performed according to the protocol as previously described (Ishii et al., 2015; Thammaporn et al., 2016). The purified PbaA (20 μM) and PbaA/PF0014 complex (11 μM) were buffer-exchanged into 200 mM ammonium acetate, pH 8.0, by passing the proteins through a Bio-Spin 6 column (Bio-Rad). The buffer-exchanged PbaA and PbaA/PF0014 complex were immediately analyzed by nanoflow electrospray

ionization MS using gold-coated glass capillaries made in house (approximately 2–5 μL sample loaded per analysis). Under a denaturing condition, 30% (v/v) formic acid was added to the sample solution. Spectra were recorded on a SYNAPT G2-S*i* HDMS mass spectrometer (Waters, Manchester, UK) in positive ionization mode at 1.63 kV with a 150 V sampling cone voltage and source offset voltage, 0 V trap and transfer collision energy, and 5 mL/min trap gas flow. The spectra were calibrated using 1 mg/mL cesium iodide and analyzed using Mass Lynx software (Waters "Milford, Massachusetts, USA").

4.2.6 Negative staining electron microscopy

PbaA/PF0014 complex, PbaA/Trx-tagged PF0014 complex and CΔ30-PbaA/PF0014 complex were dissolved at concentrations of 1.0 mg/ml, 2.0 mg/ml and 2.1 mg/ml, respectively in buffer containing 50 mM Tris-HCl (pH 8.0), 150 mM NaCl and 2 mM DTT.

EM grid preparation and single particle negative staining images of the protein complexes were prepared according to the conventional protocol as previously described (Murata et al., 2010a; Murata et al., 2010b). Samples were imaged at room temperature using a JEOL JEM 2200FS electron microscope equipped with a field

emission gun operating at an acceleration voltage of 200 kV.

4.2.7 Solution scattering

Solution scattering experiments were performed at 20°C during irradiation. The observed SAXS intensity was corrected for background, empty cell and buffer scatterings, and transmission factors and subsequently converted to the absolute scale by GRASP software using incident beam flux. The scattering intensity was normalized by weight concentration of samples. PbaA/Trx-tagged PF0014 complex and CΔ30-PbaA/PF0014 complex were dissolved at concentrations of 1.3 mg/ml and 3.4 mg/ml, respectively in buffer containing 50 mM Tris-HCl (pH 8.0), 150 mM NaCl and 2 mM DTT.

4.3 Results

4.3.1 Native mass spectrometry of PbaA/PF0014 complex

First, I performed native MS analysis to characterize the oligomeric state of PbaA/PF0014 complex in solution. Native MS data indicated that the molecular mass determined for this complex was 444729.50±47.13 Da, which corresponds to a 10:10 complex composed of PbaA and PF0014 (with a calculated mass of 445 kDa), whereas the molecular mass for PbaA homopentamer exhibited 136895.55±5.22 Da in solution state (**Figure 4.3.1**). Under a denaturing condition with 30% (v/v) formic acid, the PbaA/PF0014 complex exhibited two ion series corresponding to the molecular masses of the PF0014 (16850 Da) and PbaA (27404 Da). Thus, I confirmed that the PbaA and PF0014 formed a complex exclusively in a 10:10 stoichiometry. I also confirmed PbaB did not form complex with PF0014 by size exclusion chromatography and native MS analysis.

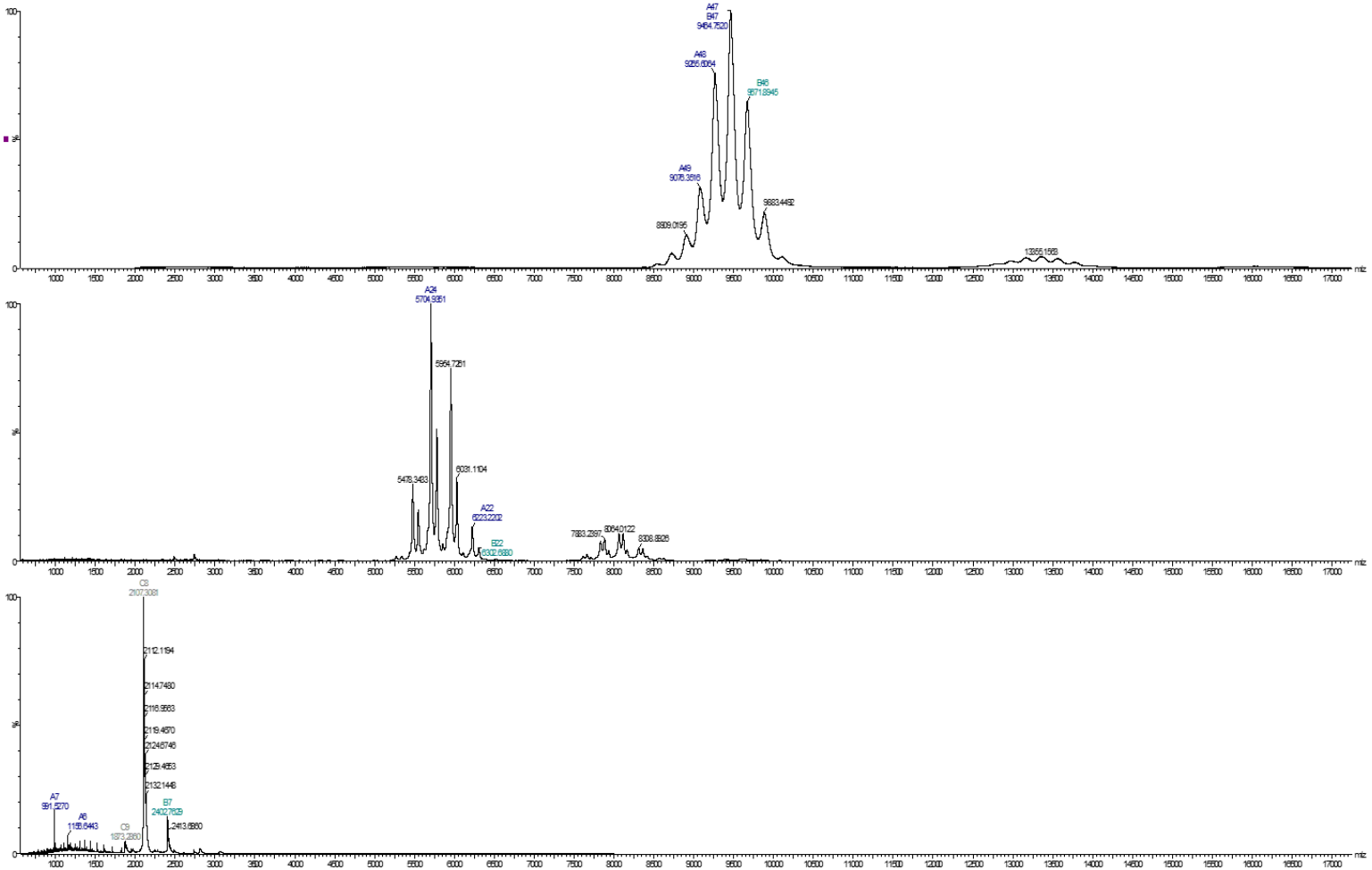

Figure 4.3.1 Mass spectra of mixtures of PbaA and PF0014 at 1:1 molar ratio (upper) and PbaA under non-denaturing conditions (midle). Under a denaturing condition with 30% (v/v) formic acid, PbaA/PF0014 complex exhibited two ion series corresponding to the molecular masses of PbaA and PF0014 (lower).

4.3.2 Three-dimensional structure of PbaA/PF0014 complex

To characterize the three-dimensional structure of the PbaA/PF0014 complex, structural analyses were performed by HS-AFM and EM. The HS-AFM data revealed that PbaA/PF0014 complex makes dumbbell-shaped structure in solution (**Figure 4.3.2**). The central pore of PbaA was closed upon complex formation of PF0014.

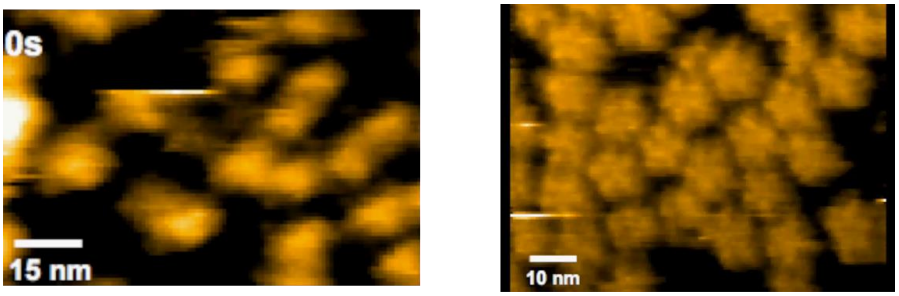

Figure 4.3.2 Typical HS-AFM images of PbaA/PF0014 complex from the side (left) and the top (right). The normal mica and the 0.1% aminosilane-treated mica were used for the side-view and the top-view, respectively.

For the high-resolution visualization of the PbaA/PF0014 complex structure, single particle negative staining images were collected (**Figure 4.3.3**). In total, 4 kinds of images were obtained with the highest particle numbers of 1206, 732, 508, and 496, respectively. These EM images showed that PbaA formed a dumbbell-like structure with PF0014 as observed in the HS-AFM analysis. To know exact positioning of PF0014, I prepared a fusion PF0014 protein in which a Trx tag was conjugated at the N-terminus. In total, 4 kinds of images of PbaA/Trx-tagged PF0014 complex were obtained with the

highest particle numbers of 2309, 2047, 1384 and 801, respectively. These EM tomograms of PbaA complexed with Trx-tagged PF0014 was almost consistent with that of the complex formed between non-tagged PbaA and PF0014 except for the spike-like image at the central part (**Figure 4.3.4**). It is suggested that this spike-like structure is probably derived from the part of Trx-tag. Namely, these structural data indicated that ten PF0014 molecules are packed between two homopentameric rings of PbaA.

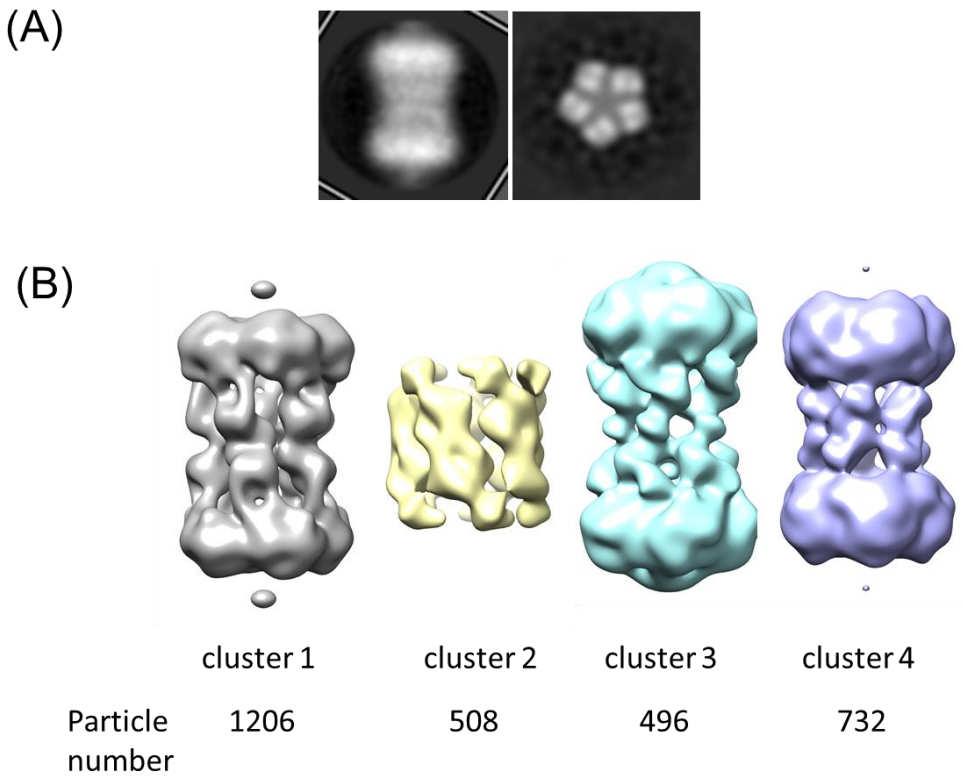

Figure 4.3.3 (A) Class averages of the PbaA/PF0014 complex from the side view (right) and the top view (left). (B) Three-dimensional EM images for PbaA/PF0014 complex were obtained by the single particle negative staining electron microscopy.

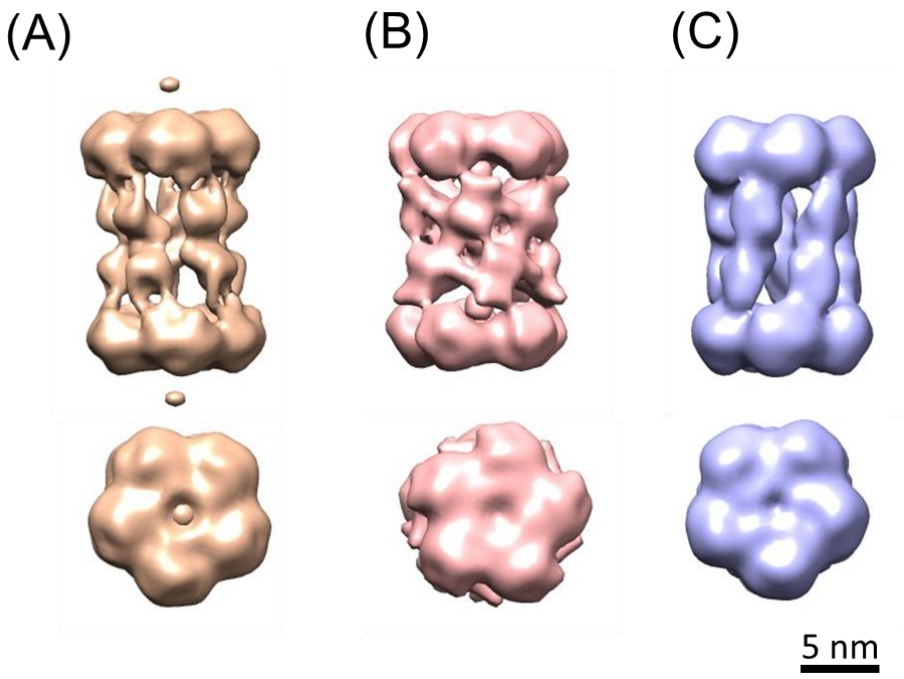

Figure 4.3.4 Three-dimensional EM images for (A) PbaA/PF0014 complex, (B) PbaA/Trx-tagged PF0014 complex, and (C) CΔ30-PbaA/PF0014 complex were obtained by the single particle negative staining electron microscopy.

The C-terminal segments of PbaA were not clearly visible in the EM map of PbaA/PF0014. Therefore, I observed EM images of CΔ30-PbaA complexed with PF0014 in order to elucidate whether or not the C-terminal segments of PbaA are involved in the complex formation. In total, 4 kinds of images of CΔ30-PbaA/PF0014 complex were obtained with the highest particle numbers of 2017, 1572, 586 and 248, respectively. Consequently, the EM images showed that a similar dumbbell-like structure was formed by the CΔ30-PbaA/PF0014 complex, indicating that the

C-terminal segments of PbaA are not involved in complex formation (**Figure 4.3.4**). I also confirmed the complex conformation of PF0014 with PbaA and CΔ30-PbaA in the SAXS measurements (**Figure 4.3.5**). Native MS data showed that the chimeric proteins $PbaA^{N230}$-$PbaB^{C13}$ and $PbaA^{N204}$-$PbaB^{C43}$ were capable of forming complexes with PF0014. All these data indicates that the C-terminal helices of PbaA are not involved in formation of the complex with PF0014.

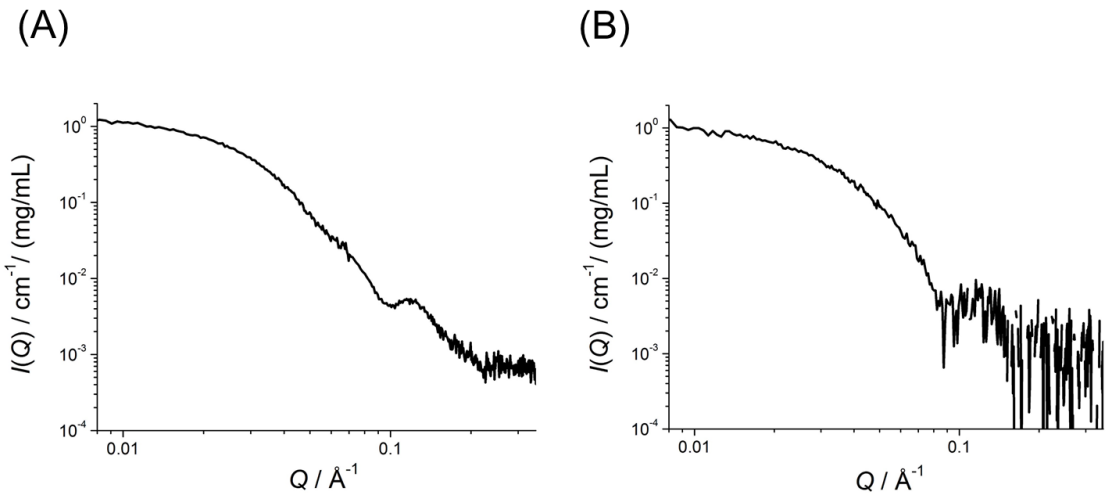

Figure 4.3.5 The experimentally obtained SAXS profiles of (A) PbaA/Trx-tagged PF0014 complex and (B) CΔ30-PbaA/PF0014 complex. The SAXS profile yielded the *Rg* values of PbaA/Trx-tagged PF0014 complex and CΔ30-PbaA/PF0014 complex as 69.6 ± 1.4 Å and 62.2 ± 0.5 Å, respectively.

4.4 Discussion

By inspection of all these data, I found that ten PF0014 protomers mediate two pentamers of PbaA, giving rise to the stable dumbbell-like complex irrespective of the C-terminal segment of PbaA. In fact, the molecular construction of this cage structure resembles a classical Greek "tholos" where the PF0014 proteins mediating the PbaA homopentameric rings mimic the columns of this unique architecture through their intermolecular interactions.

My results obtained by comparing the complex structures between wild-type PbaA and the CΔ30-PbaA mutant indicated that the PbaA C-terminal segments are dispensable for interaction with PF0014 and invisible in the EM image probably due to their mobile nature as in the case of Trx-tag artificially introduced into the N-terminus of PF0014. I have already shown that the C-terminal helices mask the hydrophobic surface of the core domains, thereby preventing the double ring formation. The PbaA/PF004 complex exhibited no further stacking even in the absence of the C-terminal helices indicating that the PF0014 proteins, instead of the C-terminal helices, conceal the hydrophobic surface of the PbaA pentameric core, liberating the C-terminal helices in the wild-type complex. This means that the two homopentameric rings of PbaA are positioned at both ends of the tholos making their hydrophobic surfaces in

contact with the inner PF0014 molecules. The crystal structure of the core domains of the PbaA homopentamer well fit into the dumbbell-plate at the ends of the EM image averaged map (**Figure 4.4.1**). Thus, I could elucidate the structural architecture of the PbaA/PF004 complex.

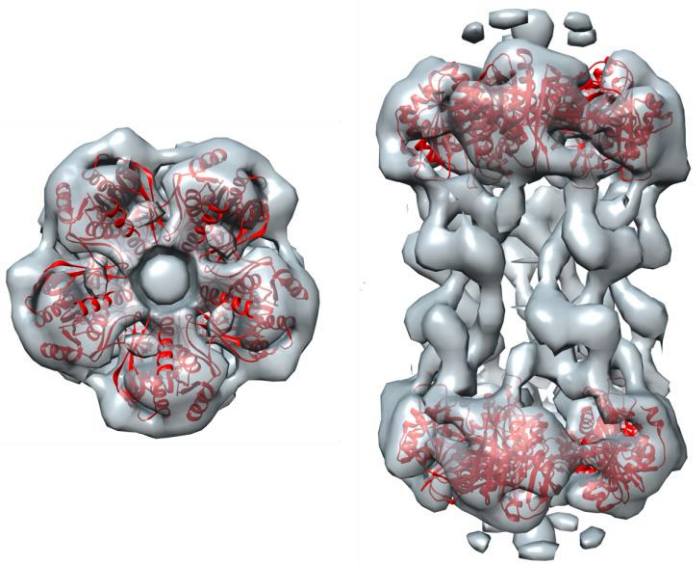

Figure 4.4.1 Tholos-like structure of PbaA/PF0014 complex. The core domain of the crystal structures of PbaA homopentamer are fitted into the dumbbell-plate at both ends of the EM maps: (left) top view, (right) side view.

Chapter 5: Summary and perspective

Chapter 5: Summary and perspective

In this study, I have characterized the three-dimensional structure of PbaA, an archaeal homolog of proteasome assembly chaperone. I have become successful in unveiling different structural designs of PbaA in comparison with its homologs despite that fact that they share a common structural fold of globular core domain and a common functional motif potentially activating the 20S proteasome. PbaA adopts a homopentameric ring structure; whereas PbaB exists as a homotetramer and their eukaryotic counterparts Pba1 and Pba2 form a heterodimer.

Moreover, by an integrative experimental approach including X-ray crystallography, SANS, SAXS, EM and HS-AFM, I could elucidate that PbaA is capable of forming a multiple structural architecture with different conformational states of its C-terminal segment under different conditions.

Under crystalline states, PbaA form a homopentameric ring with a donut-like structure as well as homodecamer form with a cage-like structure. In its homopentameric form, the C-terminal segments are highly packed inside the core part of PbaA. In contrast, in its homodecameric form, the C-terminal segments are expanded from the core part of PbaA, making anti-parallel coiled-coil interactions between the two homopentameric rings. Both these packed and extended forms refer to the fact that

PbaA can transform between the closed and open conformations by altering the orientation of the C-terminal segments which is essentially movable.

Under the solution state, the vast majority of PbaA exist as the closed form although it also exhibits the open conformation as minor form. My crystallographic data indicate that, in the closed form, the C-terminal helices mask the hydrophobic surface of the core domain. Indeed, the truncation of the C-terminal segments results in formation of the stacked double ring architecture most probably mediated by the interaction between the exposed hydrophobic surfaces.

The different conformational states of the C-terminal segments between PbaA and PbaB explain their distinct functions. Namely, the PbaA homopentamer cannot bind the 20S proteasome as its C-terminal segments are primarily packed inside whereas the the PbaB homotetramer can activate the 20S proteasome through its extended C-terminal segments. My created chimeric proteins comprising the pentameric PbaA scaffold and the extended C-terminal segments are capable of activating the 20S proteasome. This achievement suggests that the orientation of the C-terminal segments can be altered by disrupting their hydrophobic interactions with the core domains or by introducing electrostatic repulsion among the C-terminal segments in the homopentameric ring.

My study underscores the idea that the functional binding partner of PbaA in

archaeal cells is not the proteasome but the PF0014 protein. I revealed that PbaA and PF0014 form a 10:10 complex having a tholos-like architecture. It is plausible that the PF0014 proteins bind the hydrophobic surface of the homopentameric core of PbaA expelling the PbaA C-terminal segments, which become mobile in the complex. Although the function of this protein tholos remains unexplored, the structural architecture suggests its capability for molecular encapsulation in archaeal cells.

The multiple structural architectures involving PbaA suggest its novel function independent of the assembly and activation of the 20S proteasome. The various assembly states of PbaA can provide a new direction to think why this complexity does exist or whether it has some sophisticated novel functional roles in the living system. For example, because of its conformational versatility, PbaA may form different oligomeric structures in response to environmental changes surrounding the organism.

In summary, this study revealed unique, multiple structural architectures involving the archaeal homologs of proteasome assembly chaperones, giving new insights into the structural design underlying the dynamic ordering of biomolecules that have internal complexities for the creation of integrated functions.

List of references

Ando, T., Uchihashi, T., and Fukuma, T. (2008). High-speed atomic force microscopy for nano-visualization of dynamic biomolecular processes. Prog Surf Sci *83*, 337-437.

Baumeister, W., Walz, J., Zuhl, F., and Seemuller, E. (1998). The proteasome: paradigm of a self-compartmentalizing protease. Cell *92*, 367-380.

Chothia, C., and Lesk, A.M. (1986). The relation between the divergence of sequence and structure in proteins. The EMBO journal *5*, 823-826.

Coux, O., Tanaka, K., and Goldberg, A.L. (1996). Structure and functions of the 20S and 26S proteasomes. Annu Rev Biochem *65*, 801-847.

Cowtan, K. (1994). An automated procedure for phase improvement by density modification. Joint CCP4 and ESF-EACBM Newsletter on Protein Crystallography *31*, 34-38.

Emsley, P., Lohkamp, B., Scott, W.G., and Cowtan, K. (2010). Features and development of Coot. Acta Crystallogr D Biol Crystallogr *66*, 486-501.

Glickman, M.H. (2000). Getting in and out of the proteasome. Seminars in cell & developmental biology *11*, 149-158.

Hura, G.L., Menon, A.L., Hammel, M., Rambo, R.P., Poole, F.L., 2nd, Tsutakawa, S.E., Jenney, F.E., Jr., Classen, S., Frankel, K.A., Hopkins, R.C., *et al.* (2009). Robust, high-throughput solution structural analyses by small angle X-ray scattering (SAXS). Nat Methods *6*, 606-612.

Ishii, K., Noda, M., Yagi, H., Thammaporn, R., Seetaha, S., Satoh, T., Kato, K., and Uchiyama, S. (2015). Disassembly of the self-assembled, double-ring structure of proteasome alpha7 homo-tetradecamer by alpha6. Sci Rep *5*, 18167.

Kock, M., Nunes, M.M., Hemann, M., Kube, S., Dohmen, R.J., Herzog, F., Ramos, P.C., and Wendler, P. (2015). Proteasome assembly from 15S precursors involves major conformational changes and recycling of the Pba1-Pba2 chaperone. Nat Commun *6*,

6123.

Kumoi, K., Satoh, T., Murata, K., Hiromoto, T., Mizushima, T., Kamiya, Y., Noda, M., Uchiyama, S., Yagi, H., and Kato, K. (2013). An archaeal homolog of proteasome assembly factor functions as a proteasome activator. PLoS One *8*, e60294.

Kusmierczyk, A.R., Kunjappu, M.J., Kim, R.Y., and Hochstrasser, M. (2011). A conserved 20S proteasome assembly factor requires a C-terminal HbYX motif for proteasomal precursor binding. Nature structural & molecular biology *18*, 622-629.

Langer, G., Cohen, S.X., Lamzin, V.S., and Perrakis, A. (2008). Automated macromolecular model building for X-ray crystallography using ARP/wARP version 7. Nat Protoc *3*, 1171-1179.

Letoquart, J., van Tran, N., Caroline, V., Aleksandrov, A., Lazar, N., van Tilbeurgh, H., Liger, D., and Graille, M. (2015). Insights into molecular plasticity in protein complexes from Trm9-Trm112 tRNA modifying enzyme crystal structure. Nucleic acids research *43*, 10989-11002.

Liu, G., Li, Z., Chiang, Y., Acton, T., Montelione, G.T., Murray, D., and Szyperski, T. (2005). High-quality homology models derived from NMR and X-ray structures of E. coli proteins YgdK and Suf E suggest that all members of the YgdK/Suf E protein family are enhancers of cysteine desulfurases. Protein Sci *14*, 1597-1608.

Lovell, S.C., Davis, I.W., Arendall, W.B., 3rd, de Bakker, P.I., Word, J.M., Prisant, M.G., Richardson, J.S., and Richardson, D.C. (2003). Structure validation by Calpha geometry: phi,psi and Cbeta deviation. Proteins *50*, 437-450.

Lowe, J., Stock, D., Jap, B., Zwickl, P., Baumeister, W., and Huber, R. (1995). Crystal structure of the 20S proteasome from the archaeon T. acidophilum at 3.4 A resolution. Science *268*, 533-539.

Luo, Q., Dong, Z., Hou, C., and Liu, J. (2014). Protein-based supramolecular polymers: progress and prospect. Chem Commun (Camb) *50*, 9997-10007.

Maharaj, K.A., Que, N.L., Hong, F., Huck, J.D., Gill, S.K., Wu, S., Li, Z., and Gewirth,

D.T. (2016). Exploring the Functional Complementation between Grp94 and Hsp90. PLoS One *11*, e0166271.

Menon, A.L., Poole, F.L., 2nd, Cvetkovic, A., Trauger, S.A., Kalisiak, E., Scott, J.W., Shanmukh, S., Praissman, J., Jenney, F.E., Jr., Wikoff, W.R., *et al.* (2009). Novel multiprotein complexes identified in the hyperthermophilic archaeon Pyrococcus furiosus by non-denaturing fractionation of the native proteome. Mol Cell Proteomics *8*, 735-751.

Murata, K., Liu, X., Danev, R., Jakana, J., Schmid, M.F., King, J., Nagayama, K., and Chiu, W. (2010a). Zernike phase contrast cryo-electron microscopy and tomography for structure determination at nanometer and subnanometer resolutions. Structure *18*, 903-912.

Murata, K., Nishimura, S., Kuniyasu, A., and Nakayama, H. (2010b). Three-dimensional structure of the alpha1-beta complex in the skeletal muscle dihydropyridine receptor by single-particle electron microscopy. J Electron Microsc (Tokyo) *59*, 215-226.

Murata, S., Yashiroda, H., and Tanaka, K. (2009). Molecular mechanisms of proteasome assembly. Nature reviews Molecular cell biology *10*, 104-115.

Murshudov, G.N., Vagin, A.A., and Dodson, E.J. (1997). Refinement of macromolecular structures by the maximum-likelihood method. Acta Crystallogr D Biol Crystallogr *53*, 240-255.

Ness, S.R., de Graaff, R.A., Abrahams, J.P., and Pannu, N.S. (2004). CRANK: new methods for automated macromolecular crystal structure solution. Structure *12*, 1753-1761.

Otwinowski, Z., and Minor, W. (1997). Processing of X-ray diffraction data collected in oscillation mode. Methods in Enzymology *276*, 307-326.

Rabl, J., Smith, D.M., Yu, Y., Chang, S.C., Goldberg, A.L., and Cheng, Y. (2008). Mechanism of gate opening in the 20S proteasome by the proteasomal ATPases. Mol Cell *30*, 360-368.

Ramos, P.C., and Dohmen, R.J. (2008). PACemakers of proteasome core particle assembly. Structure *16*, 1296-1304.

Smith, D.M., Chang, S.C., Park, S., Finley, D., Cheng, Y., and Goldberg, A.L. (2007). Docking of the proteasomal ATPases' carboxyl termini in the 20S proteasome's alpha ring opens the gate for substrate entry. Mol Cell *27*, 731-744.

Sprangers, R., and Kay, L.E. (2007). Quantitative dynamics and binding studies of the 20S proteasome by NMR. Nature *445*, 618-622.

Stadtmueller, B.M., and Hill, C.P. (2011). Proteasome activators. Mol Cell *41*, 8-19.

Stadtmueller, B.M., Kish-Trier, E., Ferrell, K., Petersen, C.N., Robinson, H., Myszka, D.G., Eckert, D.M., Formosa, T., and Hill, C.P. (2012). Structure of a proteasome Pba1-Pba2 complex: implications for proteasome assembly, activation, and biological function. J Biol Chem *287*, 37371-37382.

Subedi, G.P., Satoh, T., Hanashima, S., Ikeda, A., Nakada, H., Sato, R., Mizuno, M., Yuasa, N., Fujita-Yamaguchi, Y., and Yamaguchi, Y. (2012). Overproduction of anti-Tn antibody MLS128 single-chain Fv fragment in Escherichia coli cytoplasm using a novel pCold-PDI vector. Protein expression and purification *82*, 197-204.

Tanaka, K. (2009). The proteasome: overview of structure and functions. Proc Jpn Acad Ser B Phys Biol Sci *85*, 12-36.

Thammaporn, R., Ishii, K., Yagi-Utsumi, M., Uchiyama, S., Hannongbua, S., and Kato, K. (2016). Mass Spectrometric Characterization of HIV-1 Reverse Transcriptase Interactions with Non-nucleoside Reverse Transcriptase Inhibitors. Biol Pharm Bull *39*, 450-454.

Unno, M., Mizushima, T., Morimoto, Y., Tomisugi, Y., Tanaka, K., Yasuoka, N., and Tsukihara, T. (2002). The structure of the mammalian 20S proteasome at 2.75 A resolution. Structure *10*, 609-618.

Wani, P.S., Rowland, M.A., Ondracek, A., Deeds, E.J., and Roelofs, J. (2015). Maturation of the proteasome core particle induces an affinity switch that controls

regulatory particle association. Nat Commun *6*, 6384.

Acknowledgements

"Every scientific journey starts with a great imagination, but it is the people in this journey who nourish the imagination time to time to make it a great success." Getting PhD degree in just 3 years and 6 month has been an amazing and adventurous journey for me. With the grace of God, I have come in contact with several people who I wish to acknowledge here.

First and foremost, I am extremely grateful to my supervisor, Professor Koichi Kato, for his guidance, discussions and brainstorming sessions throughout my PhD. His scientific proficiency helped me at various stages of my research especially during the concept defining stage. I am truly thankful for all his time and efforts he devoted for my project. He has taught me, how to be an excellent scientist and set a path for me to become outstanding professor.

Next, I would like to extend my sincere gratitude to Dr. Maho Yagi-Utsumi from Institute for Molecular Science (IMS) for her valuable insights and brilliant ideas. I have learned many experimental techniques from her. Her comments and suggestions have helped me reaching perfection in every page of my thesis. She will always be a great inspiration for me.

I am extremely fortunate and thankful that I have been guided by Dr. Tadashi Satoh

from Nagoya City University (NCU). He guided me in learning various valuable experimental skills of structural biology. I had a great experience with him while performing X-ray diffraction experiment in Photon Factory as well as in SPring-8. He has also guided me in writing my first manuscript.

I would like to acknowledge Dr. Takumi Yamaguchi and Dr. Saeko Yanaka (IMS) for their valuable comments and experimental help. I would also like to extend my gratitude to Dr. Hirokazu Yagi (NCU) for his kind help during my early stage of PhD. I am grateful to my lab mates in NCU who have always been a great source of support for me.

Here I would like to express my gratitude to my lab alumni and current members including Dr. Ying Zhang, Dr. Tong Zhu, Dr. Satoshi Ninagawa, Dr. Tatsuya Suzuki, Mr. Gengwei Yan, Ms. Rina Yogo, Ms. Methanee Hiranyakorn and Mr. Kriangsak Faikhruea.

Dr. Supaporn Seetaha, Dr. Ratsupa Thammaporn, Dr. Pornthip Boonsri and Ms. Tuanjai Somboon who have helped me in learning many experimental skills. I had a great time with them and I will cherish all the moments we have spent together and their friendship as an asset.

I would also like to appreciate all the help provided by technicians and secretaries of

both IMS and NCU, including Ms. Kumiko Hattori, Ms. Hiroe Naito, Ms. Tomo Okada, Ms. Kiyomi Senda, Ms. Mariko Suzuki, Ms. Kei Tanaka, Ms.Kazue Ohnishi and Ms. Yukiko Isono.

In regard to the collaborators, I thank Dr. Kazuyoshi Murata and Dr. Chihong Song from National Institute for Physiological Sciences (NIPS) for their help in measurement from electron microscope; Dr. Masaaki Sugiyama from Kyoto University Research Reactor Institute for his guidance during SAXS measurement; Dr. Takayuki Uchihashi and Mr. Toshiya Kozai from Kanazawa University for their guidance and help in HS-AFM measurement; Dr. Kentero Ishii from Okazaki Institute for Integrative Bioscience and Dr. Susumu Uchiyama from Osaka University for their help in native mass measurement.

I sincerely appreciate the examiners of my thesis Prof. Ryota Iino, Prof. Yuji Furutani, Prof. Hironari Kamikubo and Prof. Nobuyasu Koga for their precious time and valuable comments.

Special and big thanks to all my friends in Okazaki. I have really enjoyed a quality time with Ms. Saori Kikuchihara (NIPS) and Mr. Liechi Zhang (NIBB). Furthermore, a great thank to my best friend Dr. Rupali Gupta (NIPS), who has been very supporting and caring for me during my stay in Okazaki.

Last but not the least I would like to thank my father Mr. Ratan Kumar Sikdar and my mother Mrs. Ratna Sikdar for their encouragement in all my pursuits. They have given me enough inclination to always follow my dreams. My friends in India, Ms. Keerti Rawat, Mr. Kautilya Kumar Jena, Mrs. Swati Gupta and Mrs. Preeti Khandelwal are those people who have always given me required level of motivation to finish my PhD. Finally I am really obliged to Mr. Ashok Gupta and Mrs. Sunita Gupta for taking care of me like their own kid and for their great support.